Computers and Structures 329 (2026) 108287

Contents lists available at ScienceDirect

Computers and Structures

journal homepage: www.elsevier.com/locate/cas

A novel generalized Bloch mode synthesis combined with the wave-based finite element method for modeling acousto-elastic periodic structures with strong fluid–structure interaction

Vinícius M. de S. Santos[a,b], Thiago de P. Sales[a,*], Morvan Ouisse[b]

[a] Mechanical Engineering Division, Aeronautics Institute of Technology, Praça Marechal Eduardo Gomes, 50 - Vila das Acácias, São José dos Campos, 12228-900, SP, Brazil

[b] Université Marie et Louis Pasteur, SUPMICROTECH, CNRS, Institut FEMTO-ST, Besançon, F-25000, France

ARTICLE INFO

Keywords:
Fluid–structure interaction
Periodic structures
Wave-based finite element method
Generalized Bloch mode synthesis
Modal assurance criterion
Model order reduction

ABSTRACT

This paper addresses the modeling of acousto-elastic periodic structures with strong fluid–structure interaction, i.e., lattices in which both solid materials and heavy fluids coexist, and their mutual interactions cannot be neglected. Modeling is conducted with a single unit cell of the lattice using a novel Generalized Bloch Mode Synthesis combined with the Wave-based Finite Element Method (WFEM). Reduced-order unit cell models are derived through a multi-step model order reduction (MOR) procedure, duly accounting for the coupled dynamic behavior at fluid–structure interfaces and enabling exact enforcement of the Bloch–Floquet theorem. These reduced-order models are used within the WFEM framework to quickly obtain accurate responses, without encountering numerical issues. Various unit cell geometries are examined, ranging from simpler to more complex, with fluid confined to internal cavities or distributed throughout the lattice. Both water and mercury are considered as fluids in simulations. Results demonstrate that highly reduced unit cell models are obtained with the proposed MOR strategy; accurate solutions are achieved when the reduced-order models are combined with the WFEM; the dynamic behavior of a manufactured periodic structure with confined fluid is accurately assessed; and the modeling framework performs very well irrespective of the unit cell geometry, symmetry and fluid type.

1. Introduction

In the last two decades, there has been growing interest in the dynamic behavior of periodic structures, as they have demonstrated outstanding performance in shaping wave propagation, functioning as wave filters [1], noise reducers [2], broadband vibration suppressors [3], advanced energy localizers [4], and more [5]. A variety of methods are currently available for modeling such structures, including the Finite Element Method (FEM), Wave-based FEM (WFEM), Plane Wave Expansion (PWE), spectral element method, among others [6]. The choice among these methods depends on factors such as unit cell complexity, desired accuracy, computational cost, and inherent limitations—an insufficient number of plane waves in the PWE may lead to unphysical flat band structures [7], whereas the analysis of systems that deviate from perfect periodicity may require stochastic methods [8]. Overall, the FEM remains widely used to model periodic structures because it can accommodate intricate unit cell geometries, arbitrary boundary conditions (BCs), mixed materials and phases, nonlinear behavior [9–11], and it is readily available in many software. Unfortunately, FEM requires discretizing the entire periodic structure being analyzed, often resulting in significant computational burden, especially when large-scale periodic structures or systems with many degrees of freedom (DoFs) are addressed.

On the other hand, within the WFEM framework, a single unit cell of the lattice needs to be considered, implying that not only does the model size decrease significantly, but the computational cost for performing simulations becomes virtually independent of the structure's extent. As the WFEM builds upon the FEM, it can handle periodic structures with arbitrary complexity. In addition, vibrations are understood as a wave propagation phenomenon in the WFEM, governed by the so-called *wavemodes* [12–14], meaning that, in theory, a reduced set of wavemodes might be sufficient for an accurate description of wave propagation, further reducing computational time. This latter feature, however, can prove itself troublesome, as a WFEM basis with an insufficient number of Bloch wave vectors may lead to spurious results, such as inverted resonance peaks and "artificial/fictitious" damping [15].

* Corresponding author.
Email addresses: vinicius.santos@ga.ita.br (V.M.S. Santos), tpsales@ita.br (T.P. Sales), morvan.ouisse@femto-st.fr (M. Ouisse).

https://doi.org/10.1016/j.compstruc.2026.108287
Received 2 February 2026; Accepted 14 May 2026

Although the WFEM is quite attractive for modeling periodic structures, it can be prohibitive in certain cases due to high computational cost and numerical issues [12,16]. A large number of DoFs in a unit cell model increases the complexity of solving wave-domain equations and ill-conditioning may arise when computing high-order evanescent wavemodes [17]. To address these issues, unit cell reduced-order models can be derived, prior to consideration of the WFEM. Inspired by the seminal works of Hurty [18] and Craig Jr. and Bampton [19], model reduction techniques have been developed to accelerate and improve the analysis of periodic structures. Krattiger and Hussein [20], for instance, introduced the Bloch Mode Synthesis (BMS) for computing band diagrams, with the reduction of boundary DoFs relying on system-level characteristic constraint (S-CC) modes. Four years later, the same authors developed the Generalized BMS (GBMS), in which local-level characteristic constraint (L-CC) modes replaced the S-CC ones [21].

Palermo and Marzani [22] augmented the BMS to calculate complex band structures. Aladwani [23] extended the BMS to electroelastic metamaterials with piezoelectric resonant shunt circuits. Aladwani et al. [24] further developed the BMS for non-classically damped phononic materials. Jiang et al. [25] improved the BMS by introducing the Hybrid BMS (HBMS). Cool et al. [26] extended the BMS and GBMS to calculate dispersion curves of vibroacoustic periodic structures. Xi et al. [27] introduced the GBMS with algebraic condensation (GBMS-AC). Zhu et al. [28] developed an Improved GBMS method equally using algebraic condensation (IGBMS-AC) and multi-level reduction. More recently, Santos et al. [17] proposed an improvement to the GBMS involving the determination of interface local modes taking into account the global behavior of one unit cell, leading to enhanced accuracy for the method.

Despite the significant advances in BMS-based methods, their application to acousto-elastic periodic structures with strong fluid–structure interaction, such as flexible media confining heavy fluids like water, mercury, etc., remains an open problem that has never been addressed before. It is well known that model-order reduction (MOR) of vibro-acoustic problems can be challenging and often suffers from convergence issues [29–32]. When it comes to acousto-elastic periodic structures with strong fluid–structure interaction, the situation worsens, with convergence becoming more difficult to achieve and reduced-order models becoming less reliable. Classical MOR approaches that employ uncoupled bases for MOR, as well as more elaborate techniques based on augmented bases such as those incorporating static terms [30] and/or quasi-static vectors [32], frequently used in vibro-acoustics, often fail in the derivation of reduced-order models. Wei et al. [33] recently recognized challenges in band structure calculations for systems involving fluid–structure interactions. Aladwani et al. [34] observed inaccuracies in the forced response prediction of a plate with embedded acoustic resonators when uncoupled bases were used for MOR. Later, Aladwani et al. [23] similarly reported inaccuracies in band structure calculations caused by neglecting proper coupling conditions, in this case, between structural and electrical parameters in electroelastic metamaterials.

Considering the previous exposition, this work extends the GBMS to enable its use for the analysis of acousto-elastic periodic structures with strong fluid–structure interaction. One-dimensional wave propagation is considered for simplicity, but the novel GBMS strategy also applies to structures showing two- or three-dimensional periodicity, provided that the distinct DoF partitioning required by the Bloch–Floquet theorem is respected. First, uncoupled structural and acoustic internal DoFs of a unit cell are reduced using the Craig–Bampton (CB) method, while preserving internal DoFs at the fluid–structure interface (FSI) [35] and unit cell boundaries. Then, internal FSI DoFs are reduced using L-CC model reduction [21], but employing three sets of Ritz vectors that account for local modes (LMs), rigid-body modes (RBMs), and low-frequency flexible-body modes (FBMs) [36]. Boundary DoFs are subsequently reduced via L-CC modes, adopting projection matrices that account for the dynamic behavior of the uncoupled and/or coupled DoFs located at the unit cell interfaces. While dispersion curves computed using the novel GBMS apply only to infinite periodic systems, the WFEM is employed to obtain forced responses of finite acousto-elastic structures. A summary of all steps proposed for investigating acousto-elastic periodic structures with the novel GBMS and the WFEM is shown in Fig. 1. Although two-dimensional unit cells are shown in Fig. 1 for illustration purposes, this work focuses on three-dimensional geometries afterward. The introduced MOR approach is, however, also applicable to structures described by two-dimensional finite element models, such as those in plane-stress or plane-strain states [37].

At this stage, it should be highlighted that the modeling framework proposed in this paper is intended for acousto-elastic periodic structures fully filled with fluid, irrespective of the shape of the cavity holding the fluid. The consideration of lattices composed of unit cells that are partially filled falls outside the scope of the present work, as such configurations may involve i) non-uniform fluid distribution within unit cells, with cavities forming multiple partially filled disjoint domains; ii) bubble formation due to the presence of air or voids simultaneously with heavier fluids within unit cells; iii) capillarity effects arising from the fluid's surface tension; and iv) linear or non-linear fluid sloshing. The MOR approach introduced in this work within the GBMS can, however, be applied to other types of acousto-elastic systems, not only unit cells, such as joints and/or defects connecting waveguides, components used in component mode synthesis (CMS), and general non-periodic acousto-elastic structures. In addition, it must be stressed that the model reduction theory presented throughout this paper concerns periodic structures that encompass strong fluid–structure interaction, such that influences of the fluid on the underlying elastic medium, and vice versa, are not negligible. It can, however, be equally applied to systems with light fluid–structure interaction, although simpler strategies exist in the literature for such cases, like techniques that employ uncoupled bases for MOR.

The main contributions of this work are as follows:

I. The GBMS is extended to acousto-elastic periodic structures showcasing strong fluid–structure interaction;
II. Interface/boundary reduction is addressed for unit cells exhibiting structural and fluid DoFs at their boundaries;
III. A MAC-based procedure for discarding redundant boundary modes during interface MOR is extended to acousto-elastic periodic structures;
IV. The proposed modeling framework is validated numerically and experimentally through the analysis of a periodic-like structure with confined fluid, including the successful prediction of bending-type bandgaps.

After this introduction, modeling and MOR of acousto-elastic unit cells are discussed in Section 2, with a brief review of the WFEM being provided in Section 3. The paper's results are presented in Sections 4 and Section 5, which address both numerical simulations and experimental validation. Conclusions and references are then provided, after which an appendix helps to showcase additional results.

2. Full and reduced FE models of acousto-elastic unit cells

This section presents the MOR framework derived for unit cells of periodic structures involving strong fluid–structure interactions. Section 2.1 covers unit cell modeling. Section 2.2 addresses the reduction of uncoupled structural and acoustic internal DoFs using the CB method, while Section 2.3 covers the reduction of the remaining internal DoFs. Section 2.4 describes the reduction of boundary DoFs. Finally, Section 2.5 summarizes key aspects of the proposed MOR.

2.1. Acousto-elastic equations of motion of a unit cell

First, assume that the structural medium exhibits linear material behavior, and consider the fluid to be compressible, barotropic, inviscid, irrotational, and to exhibit linear behavior. Using solid mechanics and fluid dynamics, partial differential equations of motion describing

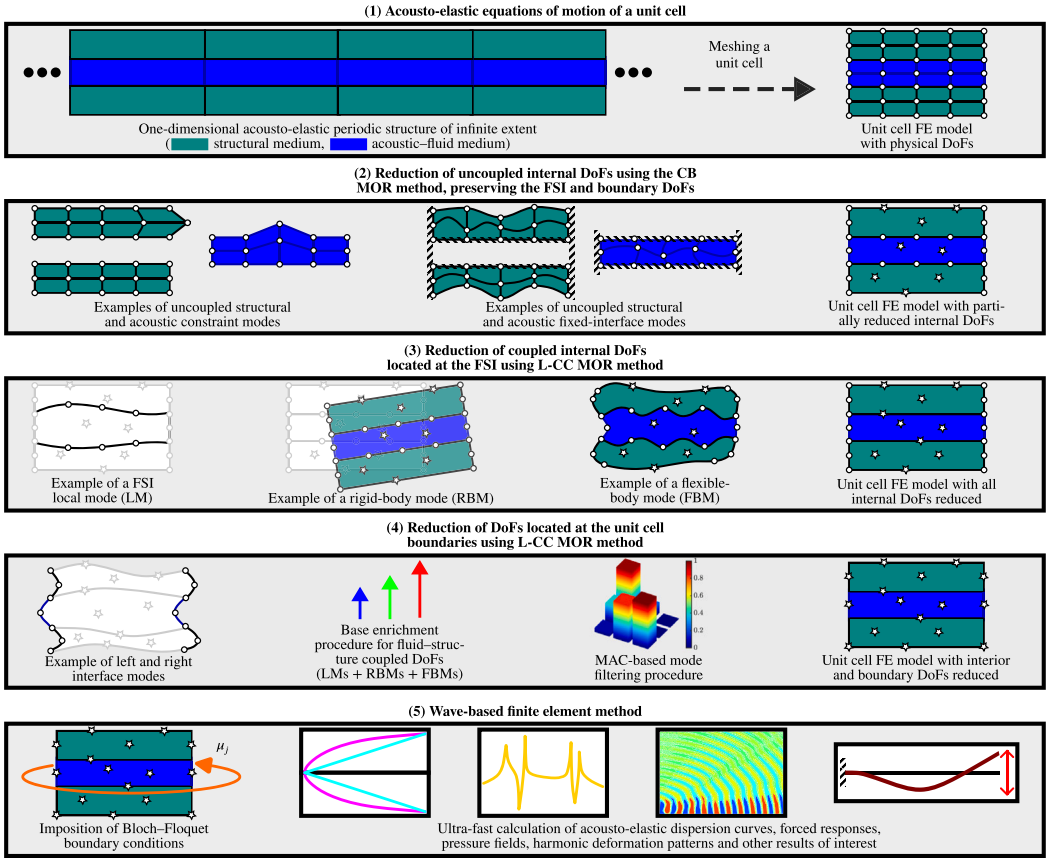

Fig. 1. Flowchart depicting the steps for analysis of acousto-elastic periodic structures showcasing strong fluid–structure interaction using the novel GBMS and WFEM.

the structural and fluid media separately can be derived. Taking into account proper fluid–structure coupling, coupled partial differential equations of motion can then be obtained. After FE discretization, the following system of ordinary differential equations of motion results for an acousto-elastic unit cell such as the one illustrated in step **(1)** of Fig. 1 [30]:

$$\begin{bmatrix} \hat{\mathbf{M}}_{\mathrm{U}} & \mathbf{0} \\ \rho\,\hat{\mathbf{R}}^{\mathrm{T}} & \hat{\mathbf{M}}_{\mathrm{P}} \end{bmatrix} \begin{Bmatrix} \ddot{\hat{\mathbf{q}}}_{\mathrm{U}}^{\dagger} \\ \ddot{\hat{\mathbf{q}}}_{\mathrm{P}}^{\dagger} \end{Bmatrix} + \begin{bmatrix} \hat{\mathbf{K}}_{\mathrm{U}} & -\hat{\mathbf{R}} \\ \mathbf{0} & \hat{\mathbf{K}}_{\mathrm{P}} \end{bmatrix} \begin{Bmatrix} \hat{\mathbf{q}}_{\mathrm{U}}^{\dagger} \\ \hat{\mathbf{q}}_{\mathrm{P}}^{\dagger} \end{Bmatrix} = \begin{Bmatrix} \hat{\mathbf{f}}_{\mathrm{U}}^{\dagger} \\ \hat{\mathbf{f}}_{\mathrm{P}}^{\dagger} \end{Bmatrix}, \tag{1}$$

where $\hat{\mathbf{q}}_{\mathrm{U}}^{\dagger}$ and $\hat{\mathbf{q}}_{\mathrm{P}}^{\dagger}$ collect structural (U) and pressure (P) DoFs, respectively; $\hat{\mathbf{f}}_{\mathrm{U}}^{\dagger}$ and $\hat{\mathbf{f}}_{\mathrm{P}}^{\dagger}$ are the corresponding load vectors; $\hat{\mathbf{M}}_j$ and $\hat{\mathbf{K}}_j$ ($j \in \{\mathrm{U}, \mathrm{P}\}$) stand for inertia and stiffness matrices; $\hat{\mathbf{R}}$ stands for the fluid–structure coupling matrix; ρ is the fluid density; $(\ )^{\mathrm{T}}$ is the transpose operator; and $(\ddot{\ })$ represents second-order derivatives with respect to time.

The global inertia and stiffness matrices appearing in Eq. (1) usually do not show good condition numbers due to the asymmetric distribution of terms resulting from fluid–structure coupling and the large difference in magnitudes caused by mixed DoFs (U and P). This can lead to numerical ill-conditioning during MOR, i.e., eigenpairs explored for MOR might be computed erroneously on account of the physical nature of the problem, as well as algorithmic or precision limitations [35,38,39]. To mitigate this issue, Eq. (1) can be rewritten using either a numerical preconditioning procedure or a non-dimensionalization strategy [35]. Following the first approach:

$$\begin{bmatrix} \hat{\mathbf{M}}_{\mathrm{U}} & \mathbf{0} \\ \gamma\rho\,\hat{\mathbf{R}}^{\mathrm{T}} & \kappa\gamma\hat{\mathbf{M}}_{\mathrm{P}} \end{bmatrix} \begin{Bmatrix} \ddot{\hat{\mathbf{q}}}_{\mathrm{U}} \\ \ddot{\hat{\mathbf{q}}}_{\mathrm{P}} \end{Bmatrix} + \begin{bmatrix} \hat{\mathbf{K}}_{\mathrm{U}} & -\kappa\hat{\mathbf{R}} \\ \mathbf{0} & \kappa\gamma\hat{\mathbf{K}}_{\mathrm{P}} \end{bmatrix} \begin{Bmatrix} \hat{\mathbf{q}}_{\mathrm{U}} \\ \hat{\mathbf{q}}_{\mathrm{P}} \end{Bmatrix} = \begin{Bmatrix} \hat{\mathbf{f}}_{\mathrm{U}} \\ \hat{\mathbf{f}}_{\mathrm{P}} \end{Bmatrix}, \tag{2}$$

where $\hat{\mathbf{q}}_{\mathrm{U}} = \hat{\mathbf{q}}_{\mathrm{U}}^{\dagger}$, $\hat{\mathbf{q}}_{\mathrm{P}} = \hat{\mathbf{q}}_{\mathrm{P}}^{\dagger}/\kappa$, $\hat{\mathbf{f}}_{\mathrm{U}} = \hat{\mathbf{f}}_{\mathrm{U}}^{\dagger}$, $\hat{\mathbf{f}}_{\mathrm{P}} = \gamma\hat{\mathbf{f}}_{\mathrm{P}}^{\dagger}$, with the coefficients κ and γ defined such that the Frobenius norms $\|\cdot\|$ of relevant block submatrices are of the same order after conditioning, i.e., [35]:

$$\kappa = \sqrt{\frac{\|\hat{\mathbf{K}}_{\mathrm{U}}\|}{\|\hat{\mathbf{R}}\|} \cdot \frac{\|\rho\hat{\mathbf{R}}\|}{\|\hat{\mathbf{M}}_{\mathrm{P}}\|}}, \qquad \gamma = \sqrt{\frac{\|\hat{\mathbf{M}}_{\mathrm{U}}\|}{\|\rho\hat{\mathbf{R}}\|} \cdot \frac{\|\hat{\mathbf{R}}\|}{\|\hat{\mathbf{K}}_{\mathrm{P}}\|}}. \tag{3}$$

To introduce the MOR theory and to analyze finite and infinite acousto-elastic periodic structures using the WFEM later, Eq. (2) is rewritten based on the DoF partitioning shown in Fig. 2. In this scheme, $\hat{\mathbf{q}}_{\mathrm{U}}$ and $\hat{\mathbf{q}}_{\mathrm{P}}$ are divided into sets of DoFs located at the left (L) and right (R) interfaces of the unit cell, as well as at its interior (I). Additionally, the DoFs located at the FSI are also distinguished, being denoted by $\hat{\mathbf{q}}_{\Gamma_j}$ (for $j \in \{\mathrm{L}, \mathrm{R}, \mathrm{I}\}$). Each of the latter sets can be further divided into those related to structural and acoustic coupled DoFs, i.e., $\hat{\mathbf{q}}_{\Gamma_{\mathrm{L}}} = \{\hat{\mathbf{q}}_{\Gamma_{\mathrm{L,U}}}^{\mathrm{T}}\ \hat{\mathbf{q}}_{\Gamma_{\mathrm{L,P}}}^{\mathrm{T}}\}^{\mathrm{T}}$,

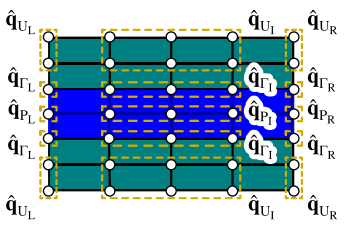

Fig. 2. Finite element mesh of a unit cell of an acousto-elastic periodic structure, showing the partitioning of DoFs based on node location (L, R, I) and medium type (U, P).

$\hat{\mathbf{q}}_{\Gamma_R} = \{\hat{\mathbf{q}}^T_{\Gamma_{R,U}}\ \hat{\mathbf{q}}^T_{\Gamma_{R,P}}\}^T$, and $\hat{\mathbf{q}}_{\Gamma_I} = \{\hat{\mathbf{q}}^T_{\Gamma_{I,U}}\ \hat{\mathbf{q}}^T_{\Gamma_{I,P}}\}^T$. Accordingly, Eq. (2) in compact form is given as:

$$\hat{\mathbf{M}}\ddot{\hat{\mathbf{q}}} + \hat{\mathbf{K}}\hat{\mathbf{q}} = \hat{\mathbf{f}}, \tag{4}$$

where vectors and matrices are partitioned according to:

$$\hat{\mathbf{q}} = \left\{\hat{\mathbf{q}}^T_{U_L}\ \hat{\mathbf{q}}^T_{P_L}\ \hat{\mathbf{q}}^T_{\Gamma_L}\ \hat{\mathbf{q}}^T_{U_R}\ \hat{\mathbf{q}}^T_{P_R}\ \hat{\mathbf{q}}^T_{\Gamma_R}\ \hat{\mathbf{q}}^T_{U_I}\ \hat{\mathbf{q}}^T_{P_I}\ \hat{\mathbf{q}}^T_{\Gamma_I}\right\}^T, \tag{5}$$

$$\hat{\mathbf{f}} = \left\{\hat{\mathbf{f}}^T_{U_L}\ \hat{\mathbf{f}}^T_{P_L}\ \hat{\mathbf{f}}^T_{\Gamma_L}\ \hat{\mathbf{f}}^T_{U_R}\ \hat{\mathbf{f}}^T_{P_R}\ \hat{\mathbf{f}}^T_{\Gamma_R}\ \hat{\mathbf{f}}^T_{U_I}\ \hat{\mathbf{f}}^T_{P_I}\ \hat{\mathbf{f}}^T_{\Gamma_I}\right\}^T, \tag{6}$$

$$\hat{\mathbf{M}} = \begin{bmatrix} \hat{\mathbf{M}}_{U_L,U_L} & \cdots & \hat{\mathbf{M}}_{U_L,\Gamma_I} \\ \vdots & \ddots & \vdots \\ \hat{\mathbf{M}}_{\Gamma_I,U_L} & \cdots & \hat{\mathbf{M}}_{\Gamma_I,\Gamma_I} \end{bmatrix}, \quad \hat{\mathbf{K}} = \begin{bmatrix} \hat{\mathbf{K}}_{U_L,U_L} & \cdots & \hat{\mathbf{K}}_{U_L,\Gamma_I} \\ \vdots & \ddots & \vdots \\ \hat{\mathbf{K}}_{\Gamma_I,U_L} & \cdots & \hat{\mathbf{K}}_{\Gamma_I,\Gamma_I} \end{bmatrix}. \tag{7}$$

2.2. Reduction of uncoupled internal DoFs using the CB MOR method, preserving the FSI and boundary DoFs

The structural and acoustic internal DoFs not on the FSI in Fig. 2 ($\hat{\mathbf{q}}_{U_I}$ and $\hat{\mathbf{q}}_{P_I}$) are uncoupled due to the FSI between them. Because of this, one can reduce both of the referred sets of internal DoFs independently of each other, by means of an adapted version of the CB MOR method, comprising step **(2)** in Fig. 1. Accordingly, the following relation between physical and partially reduced vectors of DoFs holds:

$$\hat{\mathbf{q}} = \boldsymbol{\alpha}_{CB}\tilde{\mathbf{q}}, \tag{8}$$

where:

$$\tilde{\mathbf{q}} = \left\{\hat{\mathbf{q}}^T_{U_L}\ \hat{\mathbf{q}}^T_{P_L}\ \hat{\mathbf{q}}^T_{\Gamma_L}\ \hat{\mathbf{q}}^T_{U_R}\ \hat{\mathbf{q}}^T_{P_R}\ \hat{\mathbf{q}}^T_{\Gamma_R}\ \mathbf{q}^T_{U_I}\ \mathbf{q}^T_{P_I}\ \hat{\mathbf{q}}^T_{\Gamma_I}\right\}^T, \tag{9}$$

$$\boldsymbol{\alpha}_{CB} = \begin{bmatrix} \mathbf{I} & \mathbf{0} & \mathbf{0} & \mathbf{0} & \mathbf{0} & \mathbf{0} & \mathbf{0} & \mathbf{0} & \mathbf{0} \\ \mathbf{0} & \mathbf{I} & \mathbf{0} & \mathbf{0} & \mathbf{0} & \mathbf{0} & \mathbf{0} & \mathbf{0} & \mathbf{0} \\ \mathbf{0} & \mathbf{0} & \mathbf{I} & \mathbf{0} & \mathbf{0} & \mathbf{0} & \mathbf{0} & \mathbf{0} & \mathbf{0} \\ \mathbf{0} & \mathbf{0} & \mathbf{0} & \mathbf{I} & \mathbf{0} & \mathbf{0} & \mathbf{0} & \mathbf{0} & \mathbf{0} \\ \mathbf{0} & \mathbf{0} & \mathbf{0} & \mathbf{0} & \mathbf{I} & \mathbf{0} & \mathbf{0} & \mathbf{0} & \mathbf{0} \\ \mathbf{0} & \mathbf{0} & \mathbf{0} & \mathbf{0} & \mathbf{0} & \mathbf{I} & \mathbf{0} & \mathbf{0} & \mathbf{0} \\ \boldsymbol{\Sigma}_{U_I,U_L} & \boldsymbol{\Sigma}_{U_I,P_L} & \boldsymbol{\Sigma}_{U_I,\Gamma_L} & \boldsymbol{\Sigma}_{U_I,U_R} & \boldsymbol{\Sigma}_{U_I,P_R} & \boldsymbol{\Sigma}_{U_I,\Gamma_R} & \boldsymbol{\Xi}_{U_I} & \mathbf{0} & \boldsymbol{\Sigma}_{U_I,\Gamma_I} \\ \boldsymbol{\Sigma}_{P_I,U_L} & \boldsymbol{\Sigma}_{P_I,P_L} & \boldsymbol{\Sigma}_{P_I,\Gamma_L} & \boldsymbol{\Sigma}_{P_I,U_R} & \boldsymbol{\Sigma}_{P_I,P_R} & \boldsymbol{\Sigma}_{P_I,\Gamma_R} & \mathbf{0} & \boldsymbol{\Xi}_{P_I} & \boldsymbol{\Sigma}_{P_I,\Gamma_I} \\ \mathbf{0} & \mathbf{0} & \mathbf{0} & \mathbf{0} & \mathbf{0} & \mathbf{0} & \mathbf{0} & \mathbf{0} & \mathbf{I} \end{bmatrix}, \tag{10}$$

with $\mathbf{q}_{U_I}$ and $\mathbf{q}_{P_I}$ denoting vectors of modal coordinates related to their physical counterparts $\hat{\mathbf{q}}_{U_I}$ and $\hat{\mathbf{q}}_{P_I}$; $\mathbf{I}$ representing identity matrices of appropriate sizes; $\boldsymbol{\Xi}_{U_I}$ and $\boldsymbol{\Xi}_{P_I}$ referring to matrices collecting structural and acoustic fixed-interface modes determined from:

$$\left(\hat{\mathbf{K}}_{U_I,U_I} - \hat{\lambda}_{U_{I_j}}\hat{\mathbf{M}}_{U_I,U_I}\right)\hat{\boldsymbol{\phi}}_{U_{I_j}} = \mathbf{0}, \text{ and } \left(\hat{\mathbf{K}}_{P_I,P_I} - \hat{\lambda}_{P_{I_j}}\hat{\mathbf{M}}_{P_I,P_I}\right)\hat{\boldsymbol{\phi}}_{P_{I_j}} = \mathbf{0}, \tag{11}$$

respectively, selected according to frequency-based truncation criteria, i.e., $\boldsymbol{\Xi}_{U_I}$ and $\boldsymbol{\Xi}_{P_I}$ gather $\hat{\boldsymbol{\phi}}_{U_{I_j}}$ and $\hat{\boldsymbol{\phi}}_{P_{I_j}}$, respectively, for which:

$$\hat{\lambda}^{0.5}_{U_{I_j}}/2\pi \leqslant n_{CB}f_{max} \quad \text{and} \quad \hat{\lambda}^{0.5}_{P_{I_j}}/2\pi \leqslant n_{CB}f_{max}, \tag{12}$$

where n_{CB} and f_{max} denote a multiplicative factor and the maximum frequency of analysis in Hertz, respectively[1]. Additionally, still regarding Eq. (10), structural and acoustic static/constraint modes, are calculated as follows:

$$\begin{aligned} \boldsymbol{\Sigma}_{U_I,j} &= -\hat{\mathbf{K}}^{-1}_{U_I,U_I}\hat{\mathbf{K}}_{U_I,j}, \\ \boldsymbol{\Sigma}_{P_I,j} &= -\hat{\mathbf{K}}^{-1}_{P_I,P_I}\hat{\mathbf{K}}_{P_I,j}, \end{aligned} \qquad \forall\, j \in \{U_L, P_L, \Gamma_L, U_R, P_R, \Gamma_R, \Gamma_I\}. \tag{13}$$

[1] For cases in which the smallest values of $\hat{\lambda}^{0.5}_{U_{I_j}}/2\pi$ and $\hat{\lambda}^{0.5}_{P_{I_j}}/2\pi$ are larger than $n_{CB}f_{max}$, the adoption of a single mode for each medium, related to the smallest eigenvalues, ensures that accurate reduced-order models are derived, cf. Sections 4.1.1, 4.2, 5.1 and Appendix A.

Using the relation shown in Eq. (8) in Eq. (4) and pre-multiplying the result by $\boldsymbol{\alpha}^T_{CB}$, the following reduced set of equations of motion can be obtained:

$$\tilde{\mathbf{M}}\ddot{\tilde{\mathbf{q}}} + \tilde{\mathbf{K}}\tilde{\mathbf{q}} = \tilde{\mathbf{f}}, \tag{14}$$

where $\tilde{\mathbf{M}} = \boldsymbol{\alpha}^T_{CB}\hat{\mathbf{M}}\boldsymbol{\alpha}_{CB}$, $\tilde{\mathbf{K}} = \boldsymbol{\alpha}^T_{CB}\hat{\mathbf{K}}\boldsymbol{\alpha}_{CB}$, and $\tilde{\mathbf{f}} = \boldsymbol{\alpha}^T_{CB}\hat{\mathbf{f}}$.

Although a significant reduction in the number of equations of a unit cell can be achieved by reducing the physical, uncoupled structural and acoustic internal DoFs, $\hat{\mathbf{q}}_{U_I}$ and $\hat{\mathbf{q}}_{P_I}$, to a small set of modal DoFs $\mathbf{q}_{U_I}$ and $\mathbf{q}_{P_I}$, this procedure alone is not sufficient to considerably speed up the analysis of acousto-elastic problems due to the following reasons: i) a substantial number of fluid–structure coupled equations might still be found at the interior of the unit cell, at the FSI, which can increase the computational time needed to perform the dynamic condensation of internal DoFs in the WFEM; ii) several boundary DoFs remain as physical coordinates, reducing the efficiency of the WFEM for calculating wavemodes, due to the large size of the unit cell transfer matrix. Further improvements can be obtained by locally reducing these remaining physical DoFs, which contain unnecessary high-frequency content, into a set of reduced, yet accurate, modal DoFs. This task can be performed using L-CC MOR, being addressed next in Sections 2.3 and 2.4.

2.3. Reduction of coupled internal DoFs located at the FSI using L-CC MOR method

The reduction of coupled structural and acoustic internal DoFs located at the FSI can be performed using L-CC MOR method [21], encompassing step **(3)** in Fig. 1. To accomplish this task, the following transformation is employed:

$$\tilde{\mathbf{q}} = \boldsymbol{\alpha}_{\text{L-CC}_{\Gamma_I}}\bar{\mathbf{q}}, \tag{15}$$

where $\tilde{\mathbf{q}}$ has been defined in Eq. (9), and:

$$\bar{\mathbf{q}} = \left\{\hat{\mathbf{q}}^T_{U_L}\ \hat{\mathbf{q}}^T_{P_L}\ \hat{\mathbf{q}}^T_{\Gamma_L}\ \hat{\mathbf{q}}^T_{U_R}\ \hat{\mathbf{q}}^T_{P_R}\ \hat{\mathbf{q}}^T_{\Gamma_R}\ \mathbf{q}^T_{U_I}\ \mathbf{q}^T_{P_I}\ \mathbf{q}^T_{\Gamma_I}\right\}^T, \tag{16}$$

$$\boldsymbol{\alpha}_{\text{L-CC}_{\Gamma_I}} = \begin{bmatrix} \mathbf{I} & \mathbf{0} \\ \mathbf{0} & \boldsymbol{\Psi}_{\Gamma_I} \end{bmatrix}, \tag{17}$$

with $\mathbf{q}_{\Gamma_I}$ denoting a vector of modal coordinates related to its physical counterpart, $\hat{\mathbf{q}}_{\Gamma_I}$; and $\boldsymbol{\Psi}_{\Gamma_I}$ referring to a projection matrix that collects partitions of structural and acoustic coupled modes obtained from three classes of Ritz vectors [36]:

$$\boldsymbol{\Psi}_{\Gamma_I} = \begin{bmatrix} \mathbf{L}_{\Gamma_{I,U}} & \mathbf{R}_{\Gamma_{I,U}} & \mathbf{F}_{\Gamma_{I,U}} & \mathbf{0} & \mathbf{0} & \mathbf{0} \\ \mathbf{0} & \mathbf{0} & \mathbf{0} & \mathbf{L}_{\Gamma_{I,P}} & \mathbf{R}_{\Gamma_{I,P}} & \mathbf{F}_{\Gamma_{I,P}} \end{bmatrix}. \tag{18}$$

In the above, $\mathbf{L}_{\Gamma_{I,U}}$ and $\mathbf{L}_{\Gamma_{I,P}}$ collect LMs related to the structural and acoustic internal DoFs, respectively, located at the FSI, and are determined from the eigenvectors of the following eigenvalue problem:

$$\left(\tilde{\mathbf{K}}_{\Gamma_I,\Gamma_I} - \tilde{\lambda}_{\Gamma_{I_j}}\tilde{\mathbf{M}}_{\Gamma_I,\Gamma_I}\right)\begin{Bmatrix} \tilde{\boldsymbol{\theta}}_{\Gamma_{I,U}} \\ \tilde{\boldsymbol{\theta}}_{\Gamma_{I,P}} \end{Bmatrix}_j = \mathbf{0}. \tag{19}$$

The number of modes retained in $\mathbf{L}_{\Gamma_{I,U}}$ and $\mathbf{L}_{\Gamma_{I,P}}$ follows a frequency-based truncation criterion just like the ones shown in Eq. (12), adapted to the current setting, but using $n_{\text{L-CC}_I}$ as a multiplicative factor.

It should be brought to the reader's attention that the calculation of local eigenvectors introduced herein differs from the one considered in [36]. In such reference, $(\tilde{\mathbf{K}}_{\Gamma_{I,U},\Gamma_{I,U}} - \tilde{\lambda}_{\Gamma_{I,U_j}}\tilde{\mathbf{M}}_{\Gamma_{I,U},\Gamma_{I,U}})\tilde{\boldsymbol{\theta}}_{\Gamma_{I,U\text{-}UNC_j}} = \mathbf{0}$ and $(\tilde{\mathbf{K}}_{\Gamma_{I,P},\Gamma_{I,P}} - \tilde{\lambda}_{\Gamma_{I,P_j}}\tilde{\mathbf{M}}_{\Gamma_{I,P},\Gamma_{I,P}})\tilde{\boldsymbol{\theta}}_{\Gamma_{I,P\text{-}UNC_j}} = \mathbf{0}$ are considered, such that $\tilde{\boldsymbol{\theta}}_{\Gamma_{I,U\text{-}UNC_j}}$ and $\tilde{\boldsymbol{\theta}}_{\Gamma_{I,P\text{-}UNC_j}}$ are independent of each other, in the sense that they do not account for the coupled behavior between structural and fluid DoFs at the FSI. Here, on the other hand, the Ritz vectors $\tilde{\boldsymbol{\theta}}_{\Gamma_{I,U_j}}$

and $\tilde{\theta}_{\Gamma_{\mathrm{I,P}_j}}$ collected in $\mathbf{L}_{\Gamma_{\mathrm{I,U}}}$ and $\mathbf{L}_{\Gamma_{\mathrm{I,P}}}$, respectively, are able to more accurately describe the local, coupled dynamic behavior of the structural and fluid media. Irrespective of how the referred Ritz vectors get determined, it should be noted that their absence in Eq. (18) often leads to stiffer reduced-order models, thereby compromising the MOR. Results asserting this observation are omitted in this work for the sake of brevity.

As to the second and third classes of Ritz vectors in Eq. (18), grouped in submatrices $\mathbf{R}_{\Gamma_{\mathrm{I,U}}}$, $\mathbf{F}_{\Gamma_{\mathrm{I,U}}}$, $\mathbf{R}_{\Gamma_{\mathrm{I,P}}}$, and $\mathbf{F}_{\Gamma_{\mathrm{I,P}}}$, they collect appropriate partitions of $\tilde{\boldsymbol{\phi}}_j$ ($\Gamma_{\mathrm{I,U}}$ and $\Gamma_{\mathrm{I,P}}$ DoF sets), which follow from the unit cell global-level eigenvalue problem:

$$\left(\tilde{\mathbf{K}} - \tilde{\lambda}_j \tilde{\mathbf{M}}\right) \tilde{\boldsymbol{\phi}}_j = \mathbf{0}. \tag{20}$$

By noting that $\tilde{\boldsymbol{\phi}}_j$ can be partitioned as $\tilde{\mathbf{q}}$ in Eq. (9), one can write:

$$\tilde{\boldsymbol{\phi}}_j = \begin{bmatrix} \tilde{\boldsymbol{\phi}}_{\mathrm{U}_{\mathrm{L}_j}}^{\mathrm{T}} & \tilde{\boldsymbol{\phi}}_{\mathrm{P}_{\mathrm{L}_j}}^{\mathrm{T}} & \tilde{\boldsymbol{\phi}}_{\Gamma_{\mathrm{L}_j}}^{\mathrm{T}} & \tilde{\boldsymbol{\phi}}_{\mathrm{U}_{\mathrm{R}_j}}^{\mathrm{T}} & \tilde{\boldsymbol{\phi}}_{\mathrm{P}_{\mathrm{R}_j}}^{\mathrm{T}} & \tilde{\boldsymbol{\phi}}_{\Gamma_{\mathrm{R}_j}}^{\mathrm{T}} & \tilde{\boldsymbol{\phi}}_{\mathrm{U}_{\mathrm{I}_j}}^{\mathrm{T}} & \tilde{\boldsymbol{\phi}}_{\mathrm{P}_{\mathrm{I}_j}}^{\mathrm{T}} & \tilde{\boldsymbol{\phi}}_{\Gamma_{\mathrm{I}_j}}^{\mathrm{T}} \end{bmatrix}^{\mathrm{T}}, \tag{21}$$

where:

$$\tilde{\boldsymbol{\phi}}_{\Gamma_{\mathrm{I}_j}} = \begin{bmatrix} \tilde{\boldsymbol{\phi}}_{\Gamma_{\mathrm{I,U}_j}} \\ \tilde{\boldsymbol{\phi}}_{\Gamma_{\mathrm{I,P}_j}} \end{bmatrix}. \tag{22}$$

The partitions $\tilde{\boldsymbol{\phi}}_{\Gamma_{\mathrm{I}_j}}$ of $\tilde{\boldsymbol{\phi}}_j$, for $j = 1, 2, \ldots$, can be grouped to form a modal matrix $\boldsymbol{\Phi}_{\Gamma_{\mathrm{I}}}$, from which it is easier to identify the second and third classes of Ritz vectors being considered:

$$\boldsymbol{\Phi}_{\Gamma_{\mathrm{I}}} = \left[\underbrace{\begin{matrix} \overbrace{\mathbf{R}_{\Gamma_{\mathrm{I,U}}}}^{\text{RBMs}} & \overbrace{\mathbf{F}_{\Gamma_{\mathrm{I,U}}}}^{\text{FBMs}} \\ \mathbf{R}_{\Gamma_{\mathrm{I,P}}} & \mathbf{F}_{\Gamma_{\mathrm{I,P}}} \end{matrix}}_{\text{GMs}} \right]. \tag{23}$$

Matrices $\mathbf{R}_{\Gamma_{\mathrm{I,U}}}$ and $\mathbf{R}_{\Gamma_{\mathrm{I,P}}}$ collect $\tilde{\boldsymbol{\phi}}_{\Gamma_{\mathrm{I}_j}}$ which are related to RBMs, while $\mathbf{F}_{\Gamma_{\mathrm{I,U}}}$ and $\mathbf{F}_{\Gamma_{\mathrm{I,P}}}$ gather the remaining $\tilde{\boldsymbol{\phi}}_{\Gamma_{\mathrm{I}_j}}$, which concern FBMs.

Frequency-based truncation criterion is adopted to retain the most relevant modes in $\mathbf{F}_{\Gamma_{\mathrm{I,U}}}$ and $\mathbf{F}_{\Gamma_{\mathrm{I,P}}}$, using $n_{\text{L-CC}_{\mathrm{I}}}$ again; while the number of modes included in $\mathbf{R}_{\Gamma_{\mathrm{I,U}}}$ and $\mathbf{R}_{\Gamma_{\mathrm{I,P}}}$ is limited to six RBMs plus the acoustic, Helmholtz mode. The second and third classes of Ritz vectors enable capturing how RBMs and low-frequency FBMs influence the motion of the interior subdomain of the FSI, with the zero-frequency behavior mostly influenced by the former, and the flexible behavior dominated by the latter. Note that, distinguishing RBMs from FBMs is not a strict requirement to assemble $\boldsymbol{\Psi}_{\Gamma_{\mathrm{I}}}$, as both simultaneously provide the unit cell global modes, which can be considered in Eq. (18) instead. On the other hand, distinguishing between structural and fluid DoFs is necessary.

Using Eq. (15) in Eq. (14) and pre-multiplying what results by $\boldsymbol{\alpha}_{\text{L-CC}_{\Gamma_{\mathrm{I}}}}^{\mathrm{T}}$, the following equation can be established:

$$\bar{\mathbf{M}}\ddot{\bar{\mathbf{q}}} + \bar{\mathbf{K}}\bar{\mathbf{q}} = \bar{\mathbf{f}}, \tag{24}$$

where $\bar{\mathbf{M}} = \boldsymbol{\alpha}_{\text{L-CC}_{\Gamma_{\mathrm{I}}}}^{\mathrm{T}} \tilde{\mathbf{M}} \boldsymbol{\alpha}_{\text{L-CC}_{\Gamma_{\mathrm{I}}}}$, $\bar{\mathbf{K}} = \boldsymbol{\alpha}_{\text{L-CC}_{\Gamma_{\mathrm{I}}}}^{\mathrm{T}} \tilde{\mathbf{K}} \boldsymbol{\alpha}_{\text{L-CC}_{\Gamma_{\mathrm{I}}}}$, and $\bar{\mathbf{f}} = \boldsymbol{\alpha}_{\text{L-CC}_{\Gamma_{\mathrm{I}}}}^{\mathrm{T}} \tilde{\mathbf{f}}$. At this point, all interior DoFs of the unit cell have been reduced, i.e., replaced by modal coordinates (cf. step **(3)** in Fig. 1). The reduction of boundary DoFs, possibly collecting uncoupled structural and acoustic DoFs, as well as fluid–structure coupled DoFs, as schematized in Fig. 2, is addressed next.

2.4. Reduction of DoFs located at the unit cell boundaries using L-CC MOR method

The boundary DoFs may involve uncoupled structural and fluid DoFs, as well as fluid–structure coupled DoFs in the general case (cf. Fig. 2). In other words, the fluid may not only be confined within unit cells, but may instead be shared among them through communicating channels, for example. This latter condition is of particular interest, as it allows for the design of periodic structures exhibiting acoustic (or fluidic) and elastic bandgaps simultaneously [40]. Therefore, the reduction of boundary DoFs must not only take into account the coupled dynamic behavior between fluid and structure domains, similar to step **(3)**, but also ensure the unit cell boundaries remain compatible after MOR, in the sense that the Bloch–Floquet theorem can be properly satisfied, as it is applied after the reduction of boundary DoFs. These actions are summarized in step **(4)** of Fig. 1 and discussed next.

The set of partially reduced unit cell DoFs is related to its fully reduced counterpart as follows:

$$\bar{\mathbf{q}} = \boldsymbol{\alpha}_{\text{L-CC}_{\mathrm{B}}} \mathbf{q}, \tag{25}$$

where:

$$\mathbf{q} = \begin{Bmatrix} \mathbf{q}_{\mathrm{U_L}}^{\mathrm{T}} & \mathbf{q}_{\mathrm{P_L}}^{\mathrm{T}} & \mathbf{q}_{\Gamma_{\mathrm{L}}}^{\mathrm{T}} & \mathbf{q}_{\mathrm{U_R}}^{\mathrm{T}} & \mathbf{q}_{\mathrm{P_R}}^{\mathrm{T}} & \mathbf{q}_{\Gamma_{\mathrm{R}}}^{\mathrm{T}} & \mathbf{q}_{\mathrm{U_I}}^{\mathrm{T}} & \mathbf{q}_{\mathrm{P_I}}^{\mathrm{T}} & \mathbf{q}_{\Gamma_{\mathrm{I}}}^{\mathrm{T}} \end{Bmatrix}^{\mathrm{T}}, \tag{26}$$

$$\boldsymbol{\alpha}_{\text{L-CC}_{\mathrm{B}}} = \begin{bmatrix} \boldsymbol{\Psi}_{\mathrm{U_{LR}}} & \mathbf{0} & \mathbf{0} & \mathbf{0} & \mathbf{0} & \mathbf{0} & \mathbf{0} & \mathbf{0} & \mathbf{0} \\ \mathbf{0} & \boldsymbol{\Psi}_{\mathrm{P_{LR}}} & \mathbf{0} & \mathbf{0} & \mathbf{0} & \mathbf{0} & \mathbf{0} & \mathbf{0} & \mathbf{0} \\ \mathbf{0} & \mathbf{0} & \boldsymbol{\Psi}_{\Gamma_{\mathrm{LR}}} & \mathbf{0} & \mathbf{0} & \mathbf{0} & \mathbf{0} & \mathbf{0} & \mathbf{0} \\ \mathbf{0} & \mathbf{0} & \mathbf{0} & \boldsymbol{\Psi}_{\mathrm{U_{LR}}} & \mathbf{0} & \mathbf{0} & \mathbf{0} & \mathbf{0} & \mathbf{0} \\ \mathbf{0} & \mathbf{0} & \mathbf{0} & \mathbf{0} & \boldsymbol{\Psi}_{\mathrm{P_{LR}}} & \mathbf{0} & \mathbf{0} & \mathbf{0} & \mathbf{0} \\ \mathbf{0} & \mathbf{0} & \mathbf{0} & \mathbf{0} & \mathbf{0} & \boldsymbol{\Psi}_{\Gamma_{\mathrm{LR}}} & \mathbf{0} & \mathbf{0} & \mathbf{0} \\ \mathbf{0} & \mathbf{0} & \mathbf{0} & \mathbf{0} & \mathbf{0} & \mathbf{0} & \mathbf{I} & \mathbf{0} & \mathbf{0} \\ \mathbf{0} & \mathbf{0} & \mathbf{0} & \mathbf{0} & \mathbf{0} & \mathbf{0} & \mathbf{0} & \mathbf{I} & \mathbf{0} \\ \mathbf{0} & \mathbf{0} & \mathbf{0} & \mathbf{0} & \mathbf{0} & \mathbf{0} & \mathbf{0} & \mathbf{0} & \mathbf{I} \end{bmatrix}, \tag{27}$$

with $\mathbf{q}_{\mathrm{U_L}}$, $\mathbf{q}_{\mathrm{P_L}}$, $\mathbf{q}_{\Gamma_{\mathrm{L}}}$, $\mathbf{q}_{\mathrm{U_R}}$, $\mathbf{q}_{\mathrm{P_R}}$, and $\mathbf{q}_{\Gamma_{\mathrm{R}}}$ denoting vectors of modal coordinates associated with their physical counterparts $\hat{\mathbf{q}}_{\mathrm{U_L}}$, $\hat{\mathbf{q}}_{\mathrm{P_L}}$, $\hat{\mathbf{q}}_{\Gamma_{\mathrm{L}}}$, $\hat{\mathbf{q}}_{\mathrm{U_R}}$, $\hat{\mathbf{q}}_{\mathrm{P_R}}$, and $\hat{\mathbf{q}}_{\Gamma_{\mathrm{R}}}$, respectively; and $\boldsymbol{\Psi}_{\mathrm{U_{LR}}}$, $\boldsymbol{\Psi}_{\mathrm{P_{LR}}}$, and $\boldsymbol{\Psi}_{\Gamma_{\mathrm{LR}}}$ being matrices collecting eigenvectors related to the motion of the unit cell boundaries, determined as described next. Note that, to exactly fulfill the periodicity condition required by the Bloch–Floquet theorem, $\boldsymbol{\Psi}_{\mathrm{U_{LR}}}$ is used to reduce both $\hat{\mathbf{q}}_{\mathrm{U_L}}$ and $\hat{\mathbf{q}}_{\mathrm{U_R}}$. Similarly, matrix $\boldsymbol{\Psi}_{\mathrm{P_{LR}}}$ is used for $\hat{\mathbf{q}}_{\mathrm{P_L}}$ and $\hat{\mathbf{q}}_{\mathrm{P_R}}$ DoFs, whereas $\boldsymbol{\Psi}_{\Gamma_{\mathrm{LR}}}$ is used for $\hat{\mathbf{q}}_{\Gamma_{\mathrm{L}}}$ and $\hat{\mathbf{q}}_{\Gamma_{\mathrm{R}}}$, in line with the strategy shown in [21].

Matrices $\boldsymbol{\Psi}_{\mathrm{U_{LR}}}$ and $\boldsymbol{\Psi}_{\mathrm{P_{LR}}}$ can be determined either from appropriate partitions of $\tilde{\boldsymbol{\phi}}_j$, obtained from the eigenproblem in Eq. (20) during step **(3)**, or by solving a new eigenvalue problem, stemming from Eq. (24). Because the latter option would lead to increased computational cost, the former strategy is followed in this work, such that:

$$\begin{aligned} \boldsymbol{\Psi}_{\mathrm{U_{LR}}} &= \begin{bmatrix} \tilde{\boldsymbol{\phi}}_{\mathrm{U}_{\mathrm{L}_1}} & \cdots & \tilde{\boldsymbol{\phi}}_{\mathrm{U}_{\mathrm{L}_\star}} & \tilde{\boldsymbol{\phi}}_{\mathrm{U}_{\mathrm{R}_1}} & \cdots & \tilde{\boldsymbol{\phi}}_{\mathrm{U}_{\mathrm{R}_\star}} \end{bmatrix}, \\ \boldsymbol{\Psi}_{\mathrm{P_{LR}}} &= \begin{bmatrix} \tilde{\boldsymbol{\phi}}_{\mathrm{P}_{\mathrm{L}_1}} & \cdots & \tilde{\boldsymbol{\phi}}_{\mathrm{P}_{\mathrm{L}_\star}} & \tilde{\boldsymbol{\phi}}_{\mathrm{P}_{\mathrm{R}_1}} & \cdots & \tilde{\boldsymbol{\phi}}_{\mathrm{P}_{\mathrm{R}_\star}} \end{bmatrix}, \end{aligned} \tag{28}$$

with frequency-based truncation criterion, similar to Eq. (12), applied yet again to truncate eigenvectors, $\star$ denoting the number of retained modes—$n_{\text{L-CC}_{\mathrm{B}}}$ corresponds to the adopted multiplicative factor, in this setting. Note that $\boldsymbol{\Psi}_{\mathrm{U_{LR}}}$ and $\boldsymbol{\Psi}_{\mathrm{P_{LR}}}$ collect partitions of $\tilde{\boldsymbol{\phi}}_j$ associated with both the left and right interfaces of the unit cell.

Concerning $\boldsymbol{\Psi}_{\Gamma_{\mathrm{LR}}}$, it is written similar to Eq. (18), i.e., once again considering Ritz vectors enabling accurate reduced-order models for the FSIs, but this time taking into account the influence of both the left and right interfaces of the unit cell, as for $\boldsymbol{\Psi}_{\mathrm{U_{LR}}}$ and $\boldsymbol{\Psi}_{\mathrm{P_{LR}}}$:

$$\boldsymbol{\Psi}_{\Gamma_{\mathrm{LR}}} = \begin{bmatrix} \mathbf{L}_{\Gamma_{\mathrm{L,U}}} & \mathbf{L}_{\Gamma_{\mathrm{R,U}}} & \mathbf{R}_{\Gamma_{\mathrm{L,U}}} & \mathbf{R}_{\Gamma_{\mathrm{R,U}}} & \mathbf{F}_{\Gamma_{\mathrm{L,U}}} & \mathbf{F}_{\Gamma_{\mathrm{R,U}}} & \mathbf{0} & \mathbf{0} & \mathbf{0} & \mathbf{0} & \mathbf{0} & \mathbf{0} \\ \mathbf{0} & \mathbf{0} & \mathbf{0} & \mathbf{0} & \mathbf{0} & \mathbf{0} & \mathbf{L}_{\Gamma_{\mathrm{L,P}}} & \mathbf{L}_{\Gamma_{\mathrm{R,P}}} & \mathbf{R}_{\Gamma_{\mathrm{L,P}}} & \mathbf{R}_{\Gamma_{\mathrm{R,P}}} & \mathbf{F}_{\Gamma_{\mathrm{L,P}}} & \mathbf{F}_{\Gamma_{\mathrm{R,P}}} \end{bmatrix}. \tag{29}$$

The first set of Ritz vectors, included in $\mathbf{L}_{\Gamma_{\mathrm{L,U}}}$, $\mathbf{L}_{\Gamma_{\mathrm{R,U}}}$, $\mathbf{L}_{\Gamma_{\mathrm{L,P}}}$, and $\mathbf{L}_{\Gamma_{\mathrm{R,P}}}$, is also formed considering frequency-based truncation, adopting the $n_{\text{L-CC}_{\mathrm{B}}}$ multiplicative factor, being related to the local dynamic behavior of the FSIs. They correspond to partitions of the eigenvectors determined from:

$$\begin{aligned} \left(\bar{\mathbf{K}}_{\Gamma_{\mathrm{L}},\Gamma_{\mathrm{L}}} - \bar{\lambda}_{\Gamma_{\mathrm{L}}j} \bar{\mathbf{M}}_{\Gamma_{\mathrm{L}},\Gamma_{\mathrm{L}}}\right) \begin{Bmatrix} \bar{\boldsymbol{\phi}}_{\Gamma_{\mathrm{L,U}}} \\ \bar{\boldsymbol{\phi}}_{\Gamma_{\mathrm{L,P}}} \end{Bmatrix}_j &= \mathbf{0}, \\ \left(\bar{\mathbf{K}}_{\Gamma_{\mathrm{R}},\Gamma_{\mathrm{R}}} - \bar{\lambda}_{\Gamma_{\mathrm{R}}j} \bar{\mathbf{M}}_{\Gamma_{\mathrm{R}},\Gamma_{\mathrm{R}}}\right) \begin{Bmatrix} \bar{\boldsymbol{\phi}}_{\Gamma_{\mathrm{R,U}}} \\ \bar{\boldsymbol{\phi}}_{\Gamma_{\mathrm{R,P}}} \end{Bmatrix}_j &= \mathbf{0}. \end{aligned} \tag{30}$$

On the other hand, the second and third sets of Ritz vectors, grouped in $\mathbf{R}_{\Gamma_{L,U}}$, $\mathbf{R}_{\Gamma_{R,U}}$, $\mathbf{R}_{\Gamma_{L,P}}$, $\mathbf{R}_{\Gamma_{R,P}}$, $\mathbf{F}_{\Gamma_{L,U}}$, $\mathbf{F}_{\Gamma_{R,U}}$, $\mathbf{F}_{\Gamma_{L,P}}$, and $\mathbf{F}_{\Gamma_{R,P}}$, are retrieved from RBMs and FBMs obtained via appropriate partitions of $\tilde{\boldsymbol{\phi}}_j$, determined from the eigenvalue problem in Eq. (20), similarly to the procedure adopted to assemble $\boldsymbol{\Psi}_{U_{LR}}$ and $\boldsymbol{\Psi}_{P_{LR}}$ in Eq. (28) and the way $\tilde{\boldsymbol{\phi}}_{\Gamma_{I_j}}$ provided RBMs and FBMs earlier (this time, Γ_L and Γ_R DoF sets replace Γ_I), with $n_{\text{L-CC}_B}$ considered for retaining those eigenvectors deemed most relevant. Note once again that the partitions of $\tilde{\boldsymbol{\phi}}_j$ related to the Γ_L and Γ_R DoF sets do not strictly need to be classified into RBMs and FBMs to obtain $\boldsymbol{\Psi}_{\Gamma_{LR}}$ (Eq. (29)), as the ensemble of these makes the global modes, which could be considered instead. This is analogous to the previous discussion concerning $\boldsymbol{\Psi}_{\Gamma_I}$ (Eq. (18)).

Accordingly, using Eq. (25) in Eq. (24) and pre-multiplying the obtained result by $\boldsymbol{\alpha}^{\mathrm{T}}_{\text{L-CC}_B}$, one can derive:

$$\mathbf{M}\ddot{\mathbf{q}} + \mathbf{K}\mathbf{q} = \mathbf{f}, \tag{31}$$

where $\mathbf{M} = \boldsymbol{\alpha}^{\mathrm{T}}_{\text{L-CC}_B}\bar{\mathbf{M}}\boldsymbol{\alpha}_{\text{L-CC}_B}$, $\mathbf{K} = \boldsymbol{\alpha}^{\mathrm{T}}_{\text{L-CC}_B}\bar{\mathbf{K}}\boldsymbol{\alpha}_{\text{L-CC}_B}$, and $\mathbf{f} = \boldsymbol{\alpha}^{\mathrm{T}}_{\text{L-CC}_B}\bar{\mathbf{f}}$. At this point, all unit cell physical equations, which can include dynamic content above the maximum frequency of interest, have been reduced to a set of modal equations, with the vector of DoFs $\mathbf{q}$ defined as in Eq. (26) (cf. step **(4)** in Fig. 1).

2.5. Key remarks and complementary discussions on the proposed MOR strategy

To mitigate the possibility of numerical issues within the WFEM, which is invoked in step **(5)** after deriving the unit cell reduced-order model, a filtering procedure for redundant (nearly collinear) interface modes computed in Section 2.4 is implemented using the MAC index [17], since the simplest frequency-based truncation strategy does not account for mode shape similarity. The proposed procedure involves calculating the auto-MAC for matrices defined in Eq. (28), independently, and for an auxiliary matrix defined with the non-null submatrices participating in Eq. (29), as follows:

$$\boldsymbol{\Omega} = \begin{bmatrix} \mathbf{L}_{\Gamma_{L,U}} & \mathbf{L}_{\Gamma_{R,U}} & \mathbf{R}_{\Gamma_{L,U}} & \mathbf{R}_{\Gamma_{R,U}} & \mathbf{F}_{\Gamma_{L,U}} & \mathbf{F}_{\Gamma_{R,U}} \\ \mathbf{L}_{\Gamma_{L,P}} & \mathbf{L}_{\Gamma_{R,P}} & \mathbf{R}_{\Gamma_{L,P}} & \mathbf{R}_{\Gamma_{R,P}} & \mathbf{F}_{\Gamma_{L,P}} & \mathbf{F}_{\Gamma_{R,P}} \end{bmatrix}. \tag{32}$$

Highly similar eigenvectors are then identified and discarded from $\boldsymbol{\Psi}_{U_{LR}}$, $\boldsymbol{\Psi}_{P_{LR}}$, and $\boldsymbol{\Omega}$ based on a threshold value τ defined for the filtering procedure. The relevant eigenvectors which remain in $\boldsymbol{\Omega}$ are subsequently organized back into Eq. (29), respecting the DoF partitions into structural (U) and pressure (P) sets (refer to Section 4.1.3 for more details about the implemented procedure). Alternative approaches based on singular value decomposition (SVD) might also be employed for the same purpose, i.e., to remove almost linearly-dependent vectors from a basis [41–43]. However, the singular values of the matrices of interest are sensitive to the frequency-truncation procedure applied in advance, i.e., singular values can change depending on $n_{\text{L-CC}_B}$, for example, making the selection of an appropriate SVD threshold often difficult in this setting. In addition, depending on the unit cell characteristics, the singular values may exhibit abrupt jumps in magnitude, which further complicates the selection of a suitable threshold for mode truncation [17]—particularly for criteria based on relative thresholds (e.g., normalization by the maximum singular value). As demonstrated in the aforementioned work, the MAC-based filtering technique is advantageous over SVD, as the resulting reduced-order unit cell models yield more stable and accurate harmonic forced responses, subsequently computed using the WFEM.

Afterward, it is sensible to verify whether the number of retained modes in $\boldsymbol{\Psi}_{\Gamma_I}$, $\boldsymbol{\Psi}_{U_{LR}}$, $\boldsymbol{\Psi}_{P_{LR}}$, and $\boldsymbol{\Psi}_{\Gamma_{LR}}$ (Eqs. (18), (28), and (29)) exceed the corresponding number of physical coordinates. This may occur due to: i) the need to consider three classes of Ritz vectors to reduce DoFs located at the FSI, for proper characterization of strong fluid–structure interactions [36]; and/or ii) the strategy adopted to exactly satisfy the Bloch–Floquet theorem after MOR [21]. If so, the overcomplete basis is replaced by an identity matrix of appropriate size, meaning that MOR of that set of DoFs is not performed, being therefore preserved as physical coordinates. This has been observed by the authors to be more common for unit cell models with few DoFs, where MOR is naturally not required. Otherwise, when MOR proves viable, orthogonalization must be performed to ensure non-singular transformations during MOR [21]. Thus, SVD is applied to each non-null submatrix in Eqs. (18) and (29), as well as to $\boldsymbol{\Psi}_{U_{LR}}$ and $\boldsymbol{\Psi}_{P_{LR}}$ (Eq. (28)), independently, with each being replaced by a matrix formed by its left singular vectors [17,44]—in MATLAB®, the `orth` command is a direct implementation of this procedure [45], and it is, in fact, what we have used.

It must be clear that frequency-based truncation criteria have been used to identify the bases employed for MOR throughout this work, whether in the establishment of matrices $\boldsymbol{\alpha}_{\text{CB}}$, $\boldsymbol{\alpha}_{\text{L-CC}_{\Gamma_I}}$, or $\boldsymbol{\alpha}_{\text{L-CC}_B}$. Naturally, the MAC and the orthogonalization procedures may discard some additional modes as well, even though this is not the primary purpose of the latter.

As previously noted, three projection matrices, $\boldsymbol{\alpha}_{\text{CB}}$, $\boldsymbol{\alpha}_{\text{L-CC}_{\Gamma_I}}$, and $\boldsymbol{\alpha}_{\text{L-CC}_B}$, were derived to reduce the acousto-elastic equations of motion. Alternatively, a single transformation matrix can be constructed to provide:

$$\hat{\mathbf{q}} = \boldsymbol{\alpha}\mathbf{q}, \tag{33}$$

where:

$$\boldsymbol{\alpha} = \begin{bmatrix} \boldsymbol{\Psi}_{U_{LR}} & \mathbf{0} & \mathbf{0} & \mathbf{0} & \mathbf{0} & \mathbf{0} & \mathbf{0} & \mathbf{0} & \mathbf{0} \\ \mathbf{0} & \boldsymbol{\Psi}_{P_{LR}} & \mathbf{0} & \mathbf{0} & \mathbf{0} & \mathbf{0} & \mathbf{0} & \mathbf{0} & \mathbf{0} \\ \mathbf{0} & \mathbf{0} & \boldsymbol{\Psi}_{\Gamma_{LR}} & \mathbf{0} & \mathbf{0} & \mathbf{0} & \mathbf{0} & \mathbf{0} & \mathbf{0} \\ \mathbf{0} & \mathbf{0} & \mathbf{0} & \boldsymbol{\Psi}_{U_{LR}} & \mathbf{0} & \mathbf{0} & \mathbf{0} & \mathbf{0} & \mathbf{0} \\ \mathbf{0} & \mathbf{0} & \mathbf{0} & \mathbf{0} & \boldsymbol{\Psi}_{P_{LR}} & \mathbf{0} & \mathbf{0} & \mathbf{0} & \mathbf{0} \\ \mathbf{0} & \mathbf{0} & \mathbf{0} & \mathbf{0} & \mathbf{0} & \boldsymbol{\Psi}_{\Gamma_{LR}} & \mathbf{0} & \mathbf{0} & \mathbf{0} \\ \hat{\boldsymbol{\Sigma}}_{U_I,U_L} & \hat{\boldsymbol{\Sigma}}_{U_I,P_L} & \hat{\boldsymbol{\Sigma}}_{U_I,\Gamma_L} & \hat{\boldsymbol{\Sigma}}_{U_I,U_R} & \hat{\boldsymbol{\Sigma}}_{U_I,P_R} & \hat{\boldsymbol{\Sigma}}_{U_I,\Gamma_R} & \boldsymbol{\Xi}_{U_I} & \mathbf{0} & \hat{\boldsymbol{\Sigma}}_{U_I,\Gamma_I} \\ \hat{\boldsymbol{\Sigma}}_{P_I,U_L} & \hat{\boldsymbol{\Sigma}}_{P_I,P_L} & \hat{\boldsymbol{\Sigma}}_{P_I,\Gamma_L} & \hat{\boldsymbol{\Sigma}}_{P_I,U_R} & \hat{\boldsymbol{\Sigma}}_{P_I,P_R} & \hat{\boldsymbol{\Sigma}}_{P_I,\Gamma_R} & \mathbf{0} & \boldsymbol{\Xi}_{P_I} & \hat{\boldsymbol{\Sigma}}_{P_I,\Gamma_I} \\ \mathbf{0} & \mathbf{0} & \mathbf{0} & \mathbf{0} & \mathbf{0} & \mathbf{0} & \mathbf{0} & \mathbf{0} & \boldsymbol{\Psi}_{\Gamma_I} \end{bmatrix}, \tag{34}$$

with:

$$\begin{aligned} &\hat{\boldsymbol{\Sigma}}_{i,U_j} = \boldsymbol{\Sigma}_{i,U_j}\boldsymbol{\Psi}_{U_{LR}}, \quad \hat{\boldsymbol{\Sigma}}_{i,P_j} = \boldsymbol{\Sigma}_{i,P_j}\boldsymbol{\Psi}_{P_{LR}}, \quad \hat{\boldsymbol{\Sigma}}_{i,\Gamma_j} = \boldsymbol{\Sigma}_{i,\Gamma_j}\boldsymbol{\Psi}_{\Gamma_{LR}}, \\ &\hat{\boldsymbol{\Sigma}}_{i,\Gamma_I} = \boldsymbol{\Sigma}_{i,\Gamma_I}\boldsymbol{\Psi}_{\Gamma_I}, \quad i \in \{\mathrm{U_I}, \mathrm{P_I}\}, \quad j \in \{\mathrm{L}, \mathrm{R}\}. \end{aligned} \tag{35}$$

The proposed MOR can become challenging when a unit cell contains several disjoint fluid domains, as may occur in poroelastic systems. Complications would arise because the CB MOR (step **(2)** in Fig. 1) would be required for each acoustic–fluid subdomain, and the disjoint FSIs would need to be reduced independently in step **(3)**. For cases such as the alluded one, the reduction of interior DoFs could alternatively be performed using a simpler CB method that does not preserve FSIs, where the matrices of fixed-interface modes and constraint modes would be obtained by considering:

$$\begin{aligned} &\left(\hat{\mathbf{K}}_{\mathrm{I,I}} - \hat{\lambda}_{\mathrm{I}_j}\hat{\mathbf{M}}_{\mathrm{I,I}}\right)\hat{\boldsymbol{\xi}}_j = \mathbf{0}, \quad \boldsymbol{\Sigma} = -\hat{\mathbf{K}}^{-1}_{\mathrm{I,I}}\hat{\mathbf{K}}_{\mathrm{I,B}}, \\ &\mathrm{I} \in \{\mathrm{U_I} \cup \mathrm{P_I} \cup \Gamma_\mathrm{I}\}, \quad \mathrm{B} \in \{\mathrm{U_L} \cup \mathrm{P_L} \cup \Gamma_\mathrm{L} \cup \mathrm{U_R} \cup \mathrm{P_R} \cup \Gamma_\mathrm{R}\}. \end{aligned} \tag{36}$$

Although this procedure is considerably simpler than those proposed in steps **(2)** and **(3)**, frequency-based truncation criteria often fail during MOR, necessitating either: i) the inclusion of higher-order modes, usually selected based on ad hoc frequency criteria [26,46,47]; or ii) the adoption of basis enrichment [32], which may not always be effective.

Eigenvalue problems presented in Eqs. (11), (19), (20), and (30) can be solved efficiently using iterative techniques, such as the implicitly restarted Arnoldi method, available in MATLAB® via `eigs`. The main advantage of these methods lies in their ability to handle large sparse matrices, typical of FEM-based models, while requiring less memory and computational power than direct methods. Additionally, these iterative

solvers allow for the computation of a limited number of eigensolutions, which is often desirable in MOR. Although the successive application of the previously described reduction steps results in almost fully populated system matrices, thus potentially increasing the computational cost of subsequent operations, the derived models remain small, so that no significant numerical burden is introduced.

It is worth noting that eigenvalue problems introduced previously in Eqs. (19), (20), and (30) involve asymmetric matrices. Therefore, the left and right eigenvectors related to the same eigenvalue are distinct, and the right eigenvectors are generally not orthogonal. Despite this, only the right eigenvectors have been used during MOR in this work, while ensuring their orthogonalization. Nonetheless, other approaches exploiting both left and right eigenvectors are available in the literature [48–51] and could possibly be integrated into, combined with, or replace the proposed MOR framework.

As an additional remark, it should be clarified that, in the equations of motion of acousto-elastic problems, Eq. (1), the fluid–structure coupling occurs through the coupling matrix $\hat{\mathbf{R}}$, which is responsible for making global matrices asymmetric. In this study, the reduction of fluid–structure coupled DoFs is ultimately a matter of selecting appropriate sets of Ritz vectors (cf. Sections 2.3 and 2.4). Hence, no additional equation needs to be introduced to properly enforce fluid–structure couplings during MOR, as it is already taken into account in the equations characterizing systems being studied. If fluid–structure coupling is not properly preserved, inaccurate coupled structural and acoustic FRFs will necessarily be obtained [36], i.e., fluid–structure coupled resonances may be missing from either the structural or fluid response. This behavior can be readily observed by removing either the first ($\mathbf{L}$ matrices) or the second and third ($\mathbf{R}$ and $\mathbf{F}$ matrices) classes of Ritz vectors from projection matrices (Eqs. (18) and (29)). The absence of any of these Ritz vector sets leads to a poor description of fluid–structure coupling, as local and/or global modes become neglected, which significantly affects the system responses.

Lastly, regarding fluid–structure couplings across adjacent unit cells, which may occur for acousto-elastic periodic structures incorporating communicating channels between cells, for example, compatibility between adjacent unit cells is enforced exactly in this study by adopting the same projection matrices for the reduction of the left and right boundaries [21]. In fact, the premise of "compatible boundaries" is a requirement for satisfying the Bloch–Floquet theorem afterward, which is applied considering the reduced unit cell model—recall that L-CC model reduction strategy is employed for MOR in this work. It may be possible to adopt "weak compatibility" between unit cell interfaces, as considered by Krattiger et al. [52] in CMS-based applications through the weak compatibility L-CC (WC L-CC) MOR method, but this is outside the scope of the present work. If fluid–structure coupling conditions, or any other type of coupling (fluid–fluid or structure–structure) across unit cell interfaces, are not properly satisfied, propagation constants and wave modes/wave shapes computed using full physical models and reduced-order models would differ. Since the WFEM basis relies on wave-mode expansion procedures [13], results ensuing from application of the method (frequency response functions, harmonic deformed patterns, etc.) would therefore be compromised if couplings across neighboring unit cells are not properly satisfied.

The previous two features are both taken into account in this study. Therefore, the proposed MOR methodology is able to preserve fluid–structure coupling effects whether the fluid–structure interface lies within the interior of the unit cell or at its boundaries.

3. The WFEM applied to acousto-elastic periodic structures

This section summarizes main aspects of the WFEM applied to reduced-order acousto-elastic unit cell models, corresponding to step **(5)** in Fig. 1. Further details about this wave-based modeling method can be found elsewhere [13,16,17].

It is well known that WFE models require symmetric dynamic stiffness matrices, as the method relies on symplectic orthogonality conditions [53]. Therefore, pressure DoFs $\mathbf{q}_\mathrm{P}$ may be expressed in terms of the acoustic velocity potential $\mathbf{q}_\varphi$ [54], so that Eq. (31) is rewritten as follows in the frequency domain[2]:

$$\left(-\omega^2\begin{bmatrix}\mathbf{M}_\mathrm{U} & \mathbf{0}\\ \mathbf{0} & -\rho\mathbf{M}_\mathrm{P}\end{bmatrix}+\mathrm{i}\omega\begin{bmatrix}\mathbf{0} & \rho\mathbf{R}\\ \rho\,\mathbf{R}^\mathrm{T} & \mathbf{0}\end{bmatrix}+\begin{bmatrix}\mathbf{K}_\mathrm{U} & \mathbf{0}\\ \mathbf{0} & -\rho\mathbf{K}_\mathrm{P}\end{bmatrix}\right)\begin{Bmatrix}\mathbf{Q}_\mathrm{U}\\ \mathbf{Q}_\varphi\end{Bmatrix}=\begin{Bmatrix}\mathbf{F}_\mathrm{U}\\ \mathbf{F}_\varphi\end{Bmatrix}. \quad (37)$$

In the above, $\mathbf{Q}_\mathrm{U}$, $\mathbf{Q}_\varphi$, $\mathbf{F}_\mathrm{U}$, and $\mathbf{F}_\varphi$ are frequency domain (modal) amplitudes; ω is the circular frequency, and $\mathrm{i}=\sqrt{-1}$. One should note that such a transformation does not appear necessary when FSI is not present on the unit cell boundaries, as in periodic structures with confined fluid [55], since dynamic condensation of internal DoFs renders the transfer matrix symplectic.

Eq. (37) can be manipulated, starting with the dynamic condensation of interior (modal) DoFs, followed by the establishment of the symplectic unit cell transfer matrix, $\mathbf{S}$ [13,16]. Its consideration together with the Bloch–Floquet theorem provides the standard eigenvalue problem:

$$\left(\mathbf{S}-\mu_j\mathbf{I}\right)\boldsymbol{\phi}_j=\mathbf{0},\qquad \mu_j=\exp(-\mathrm{i}k_j\Delta),\qquad j\in\{1,\ldots,2n_\mathrm{B}\}, \quad (38)$$

where μ_j is the j-th propagation constant, $\boldsymbol{\phi}_j$ is the so-called wave mode, k_j is the j-th Bloch wavenumber, Δ is the unit cell length along the direction of wave propagation, and n_B denotes the number of (modal) DoFs at the left (or right) interface of the unit cell. Due to ill-conditioning issues, alternative eigenvalue problems have been developed to replace Eq. (38) [16]—in this work, the Zhong-Williams' $\mathbf{S}+\mathbf{S}^{-1}$ strategy is employed [17]. Additionally, to sort wavenumbers in order to better visualize dispersion curves (i.e., the relation between k_j and frequency), a frequency tracking procedure that explores wave modes' orthogonality relationships needs to be implemented [15].

Wave modes $\boldsymbol{\phi}_j$ can be partitioned and organized into $\boldsymbol{\Phi}_\mathrm{Q}$, $\boldsymbol{\Phi}_\mathrm{Q}^*$, $\boldsymbol{\Phi}_\mathrm{F}$, $\boldsymbol{\Phi}_\mathrm{F}^*$, depending on direction of propagation, and propagation constants into a diagonal matrix $\boldsymbol{\mu}$. The subscripts Q and F identify those partitions associated with generalized DoFs and loads, respectively, while the superscript * distinguishes propagation in the negative direction from propagation in the positive direction [12]. These quantities can then be used to write [13]:

$$\begin{aligned}\mathbf{Q}_\mathrm{L}^{(n)}&=\boldsymbol{\Phi}_\mathrm{Q}\boldsymbol{\mu}^{n-1}\mathbf{Q}+\boldsymbol{\Phi}_\mathrm{Q}^*\boldsymbol{\mu}^{N+1-n}\mathbf{Q}^*\\&\quad+\boldsymbol{\Phi}_\mathrm{Q}\sum_{k=1}^{n-1}\boldsymbol{\mu}^{n-k-1}\mathbf{Q}_\mathrm{B}^{(k)}-\boldsymbol{\Phi}_\mathrm{Q}^*\sum_{k=n}^{N}\boldsymbol{\mu}^{k+1-n}\mathbf{Q}_\mathrm{B}^{*(k)}, \quad (39)\\ -\mathbf{F}_\mathrm{L}^{(n)}&=\boldsymbol{\Phi}_\mathrm{F}\boldsymbol{\mu}^{n-1}\mathbf{Q}+\boldsymbol{\Phi}_\mathrm{F}^*\boldsymbol{\mu}^{N+1-n}\mathbf{Q}^*\\&\quad+\boldsymbol{\Phi}_\mathrm{F}\sum_{k=1}^{n-1}\boldsymbol{\mu}^{n-k-1}\mathbf{Q}_\mathrm{B}^{(k)}-\boldsymbol{\Phi}_\mathrm{F}^*\sum_{k=n}^{N}\boldsymbol{\mu}^{k+1-n}\mathbf{Q}_\mathrm{B}^{*(k)}, \quad (40)\end{aligned}$$

where N is the number of unit cells in a finite acousto-elastic structure; $\mathbf{Q}_\mathrm{B}^{(k)}$ and $\mathbf{Q}_\mathrm{B}^{*(k)}$ are wave mode-domain amplitudes associated with externally applied loads at the kth unit cell, corresponding to positive- and negative-going waves, respectively; and $\mathbf{Q}$ and $\mathbf{Q}^*$ collect the amplitudes of wave modes that travel from the left boundary of the first cell to the right, and from the right boundary of the Nth cell to the left, respectively.

Eqs. (39) and (40) can be used in conjunction with BCs, enabling the establishment of a frequency-dependent, linear system on the unknown wave mode amplitudes $\mathbf{Q}$ and $\mathbf{Q}^*$. Structural ($\mathbf{Q}_\mathrm{U}$) and fluid ($\mathbf{Q}_\varphi$) responses can afterward be obtained for any unit cell of the lattice, whether for internal or boundary DoFs. Pressure-like responses can be directly recovered from $\mathbf{Q}_\varphi$ by considering $\mathbf{Q}_\mathrm{P}=-\mathrm{i}\omega\rho\mathbf{Q}_\varphi$.

[2] Modifications due to κ and γ should be identified and duly removed from Eq. (31) to derive Eq. (37). Nonetheless, it should be realized that the use of such constants are paramount for obtaining accurate reduced-models as given in Eq. (31).

Finally, responses in physical coordinates can be obtained using the frequency-domain version of Eq. (33), relating $\mathbf{Q}$ to $\hat{\mathbf{Q}}$ by means of the $\boldsymbol{\alpha}$ transformation matrix.

It should be clarified that Eqs. (39) and (40) presented above are rather general. Therefore, they can be used to prescribe/impose a motion or a certain pressure at interfaces through $\mathbf{Q}_{\mathrm{L}}^{(n)}$ [56]; to consider concentrated or distributed loads through $\mathbf{F}_{\mathrm{L}}^{(n)}$ at interfaces [13,17]; to account for concentrated or distributed loads applied at arbitrary locations of the periodic structure through $\mathbf{Q}_{\mathrm{B}}^{(k)}$ and $\mathbf{Q}_{\mathrm{B}}^{*(k)}$ [13]; to establish coupling conditions between neighboring, distinct waveguides [57]; etc. Although the referred equations are quite general in terms of what analyses they enable one to perform, in this study they have been particularized to address simpler conditions, i.e., involving the application of single concentrated forces, as considered in the following sections.

4. Application of the novel GBMS and WFEM to straight acousto-elastic waveguides

This section analyzes acousto-elastic periodic structures characterized by strong fluid—structure interaction using the novel GBMS and WFEM frameworks. Unlike traditional vibroacoustic analyses—where the fluid (air) has a negligible effect on structural dynamics [58]—strong fluid–structure interaction occurs when a dense fluid interacts with a highly compliant structure. This regime fundamentally alters the system's dispersion topology [59] and gives rise to coupled vibration modes, where both the structural and fluid subdomains exhibit significant, simultaneous response amplitudes [36,60]. Thus, for such conditions, MOR methods which consider, for example, uncoupled bases for the structural and acoustic-fluid domains, usually fail, as solely uncoupled eigenvectors are not able to properly predict strong fluid–structure interactions unless i) very extended bases are adopted and/or ii) basis enrichment is performed (the latter does not always work, because uncoupled bases are taken as the starting point). Accordingly, in what follows, the selection of key parameters related to the proposed MOR scheme is initially discussed, which motivates the consideration of a rather simple geometry at this stage. Then, results in terms of dispersion curves, wave modes, and harmonic deformation patterns are presented for the same introductory example. Finally, the same system is subsequently examined considering a finer mesh, with many DoFs, featuring quadratic interpolation functions, so that results are more accurate in the frequency range that is analyzed.

All results presented in this section consider an acousto-elastic unit cell with dimensions $60\,\mathrm{mm} \times 10\,\mathrm{mm} \times 30\,\mathrm{mm}$ ($\Delta = 60\,\mathrm{mm}$), which includes a central cavity measuring $60\,\mathrm{mm} \times 6\,\mathrm{mm} \times 23.6\,\mathrm{mm}$, completely filled with fluid, so that both structural and fluid domains are present throughout the cell (cf. Fig. 3). This straight acousto-elastic unit cell has been purposely chosen as the first example in this work, because i) it is relatively simple, allowing for a detailed discussion about parameters involved in the MOR process and other aspects; and ii) fluid is present both within the unit cell and at its boundaries, which allows verification of one feature of the proposed MOR strategy—more complex examples are examined later. The rather long unit cell being considered can be interpreted as a section of a straight waveguide, like a fluid-filled pipe with rectangular cross-section. Since the unit cell is straight, it would be much more appropriate to shorten it for its consideration within the WFEM framework. By doing so, MOR of internal DoFs would likely be unnecessary due to the expected small number of interior DoFs, making steps **(2)** and **(3)** of the proposed strategy unnecessary (cf. Fig. 1). It should be noted, however, that the shortening of Δ to reduce the number of interior DoFs of a unit cell is not always possible, depending on periodic features exhibited by said unit cell, cf. systems treated in Section 5 and Appendix A. In addition, reducing the unit cell length implies increasing the number of cells within the WFEM. For the example shown in Fig. 3, taking the unit cell length as $\Delta/c, c \in \mathbb{N}, c \geq 2$, would require $N = 6c$ unit cells to model the same finite structure, instead of 6, which may induce numerical issues when $c \gg 2$—since N acts in exponents in Eqs. (39) and (40). Regardless of such discussion, as in most cases a large number of internal DoFs pose challenges to the WFEM, the MOR strategy considered in our study becomes essential.

Regarding physical properties, the structural material is considered to be polylactic acid (PLA), with an elastic modulus of 1.9 GPa, a density of $1052.6\,\mathrm{kg\,m^{-3}}$, and a Poisson's ratio of 0.3, whereas the fluid is water, with a density of $998.2\,\mathrm{kg\,m^{-3}}$ and a sound speed of $1482.1\,\mathrm{m\,s^{-1}}$. Dissipation effects are considered by making the structural stiffness matrix $\mathbf{K}_{\mathrm{U}}$ in Eq. (37) complex, i.e., $\mathbf{K}_{\mathrm{U}} \leftarrow (1 + \mathrm{i}\eta)\mathbf{K}_{\mathrm{U}}$, with $\eta = 1\%$.

4.1. Selection of key parameters for model-order reduction of acousto-elastic unit cells

Several user-defined parameters are related to the MOR strategy introduced in this work and must, therefore, be carefully specified for proper use of the methodology. These include: i) n_{CB}, $n_{\text{L-CC}_{\mathrm{I}}}$, and $n_{\text{L-CC}_{\mathrm{B}}}$, cf. Sections 2.2–2.4, used to filter out eigenvectors based on their corresponding eigenvalues; ii) the number of modes retained in the projection matrices when frequency-based truncation is unable to select any mode; and iii) the MAC threshold value τ, cf. Section 2.5, used to remove redundant modes from matrices involved in the reduction of boundary DoFs (Section 2.4).

The FE mesh of the unit cell shown in Fig. 3 was generated using hexahedral elements with linear material behavior and linear interpolation functions. In order to determine suitable values for n_{CB}, $n_{\text{L-CC}_{\mathrm{I}}}$, $n_{\text{L-CC}_{\mathrm{B}}}$, and τ, bending and pressure-type frequency response functions (FRFs) were computed for a finite waveguide with $N = 6$ unit cells, assuming a harmonic force excitation applied on its left side, in the Y-direction, with the structural and acoustic (pressure) responses obtained at its right end, as indicated in Fig. 3.

All numerical simulations were conducted over the frequency range from 0 to $f_{\max} = 5000\,\mathrm{Hz}$, with a discretization of 5 Hz, unless otherwise specified. Complete wave-mode bases were always employed to compute forced responses using the WFEM. Although using a reduced basis can improve the computational efficiency of the WFEM, it may compromise

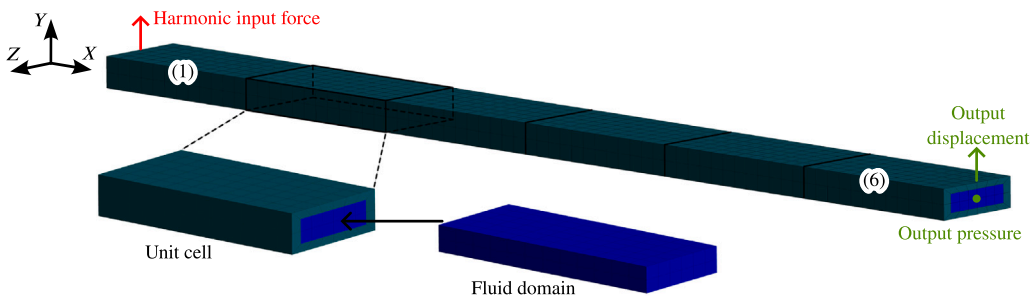

Fig. 3. Finite acousto-elastic waveguide with $N = 6$ unit cells, along with the input and output locations considered for calculating the harmonic responses shown throughout Section 4.1, and a detailed view of the long unit cell adopted for the structure.

the accuracy of forced response computations, thus requiring careful selection of wave modes [61].

4.1.1. Reduction of $\hat{\mathbf{q}}_{\mathrm{U_I}}$ and $\hat{\mathbf{q}}_{\mathrm{P_I}}$ DoFs using the CB MOR method

In accordance with step **(2)** in Fig. 1 and the theory outlined in Section 2.2, the reduction of $\hat{\mathbf{q}}_{\mathrm{U_I}}$ and $\hat{\mathbf{q}}_{\mathrm{P_I}}$ DoFs can be carried out using appropriate sets of constraint modes and fixed-interface modes, while preserving $\hat{\mathbf{q}}_{\Gamma_\mathrm{I}}$ and the boundary DoFs. Following [17], n_{CB} is set to 5; however no acoustic or structural fixed-interface modes are found below $n_{\mathrm{CB}} f_{\max} = 25\,\mathrm{kHz}$. Therefore, $\boldsymbol{\Xi}_{\mathrm{U_I}}$ and $\boldsymbol{\Xi}_{\mathrm{P_I}}$ collect individual modes whose natural frequencies are approximately 10 and 28 times greater than $f_{\max}$, respectively, corresponding to reduction factors of 528 for structural DoFs and 55 for fluid DoFs. One should stress that this large reduction of internal DoFs partially stems from the adopted unit cell length Δ being purposely selected as "large" in the present example. Notwithstanding, similar reduction factors are also seen for unit cells portraying more detailed/intricate geometry in their interior, as demonstrated in Section 5 and Appendix A. Irrespective of this, Fig. 4 shows FRFs calculated using the WFEM and the FEM, for the input and output locations in Fig. 3, where the WFEM results overlap the reference ones.

4.1.2. Reduction of $\hat{\mathbf{q}}_{\Gamma_\mathrm{I}}$ DoFs using L-CC MOR method

The reduction of $\hat{\mathbf{q}}_{\Gamma_\mathrm{I}}$ DoFs, step **(3)** in Fig. 1, follows after the reduction of $\hat{\mathbf{q}}_{\mathrm{U_I}}$ and $\hat{\mathbf{q}}_{\mathrm{P_I}}$. As discussed in Section 2.3, this reduction is performed using three sets of Ritz vectors, grouped in $\mathbf{L}_{\Gamma_{\mathrm{I},j}}$, $\mathbf{R}_{\Gamma_{\mathrm{I},j}}$, and $\mathbf{F}_{\Gamma_{\mathrm{I},j}}$, for $j \in \{\mathrm{U},\mathrm{P}\}$, determined from Eqs. (19) and (20), with $n_{\text{L-CC}_\mathrm{I}}$ adopted for frequency-truncation. Accordingly, Fig. 5 shows structural and acoustic FRFs computed using the FEM and WFEM for the configuration illustrated in Fig. 3. It reveals that accelerance magnitudes are significantly influenced by $n_{\text{L-CC}_\mathrm{I}}$, whereas pressures are only marginally affected. Specifically, referring to $\boldsymbol{\Psi}_{\Gamma_\mathrm{I}}$, cf. Eq. (18), when $n_{\text{L-CC}_\mathrm{I}}$ increases from 1.5 to 5, the number of retained structural modes rises from 40 to 134, while the number of acoustic modal DoFs changes from 38 to 128, thus showing $n_{\text{L-CC}_\mathrm{I}}$ considerably impacts the size of the reduced-order model. In particular, Fig. 5(a) shows that an insufficient number of internal modal DoFs for the FSI results in a poor approximation of the coupled acousto-elastic dynamic behavior, leading to noticeable deviations between FEM and WFEM. This is evident in Fig. 5(a), as i) various resonance peaks, which characterize strong acousto-elastic coupling, vanish or are incorrectly predicted by the reduced models; and ii) most resonance frequencies shift to the right, indicating a lack of convergence for the unit cell reduced-order model.

The value of $n_{\text{L-CC}_\mathrm{I}}$ is therefore selected as 5 for the remainder of this work, as it provides a good balance between accuracy and computational efficiency for both types of responses considered. When $n_{\text{L-CC}_\mathrm{I}} = 5$, 528 and 176 structural and acoustic physical DoFs are reduced to 134 and 128 modal DoFs, respectively, corresponding to reduction factors of approximately 4 and 1.4. Although these factors may appear small, they increase significantly when unit cell FE models with higher-order interpolation functions and smaller element sizes (i.e., converged meshes) are considered, as demonstrated in Section 4.2.

4.1.3. Reduction of DoFs located at the unit cell boundaries using L-CC MOR method

After all internal equations have been reduced, the reduction of boundary DoFs, step **(4)** in Fig. 1, takes place. The related projection matrices $\boldsymbol{\Psi}_{\mathrm{U_{LR}}}$, $\boldsymbol{\Psi}_{\mathrm{P_{LR}}}$, and $\boldsymbol{\Psi}_{\Gamma_{\mathrm{LR}}}$ are derived following the procedures outlined in Section 2.4, relying on eigenvectors from Eq. (20) (obtained previously in step **(3)**, during the reduction of internal DoFs located at the FSI) and Eq. (30). The relevant modal content in each basis is first filtered using frequency-based truncation, followed by the MAC-based procedure that discards nearly collinear modes.

As discussed in Section 2.5, the MAC-based mode filtering procedure involves computing the auto-MAC for $\boldsymbol{\Psi}_{\mathrm{U_{LR}}}$, $\boldsymbol{\Psi}_{\mathrm{P_{LR}}}$, and $\boldsymbol{\Omega}$. Accordingly, Fig. 6 shows a three-dimensional bar plot and the matrix heatmap of the auto-MAC of $\boldsymbol{\Psi}_{\mathrm{U_{LR}}}$ considering $n_{\text{L-CC}_\mathrm{B}} = 2$—similar results for $\boldsymbol{\Psi}_{\mathrm{P_{LR}}}$ and $\boldsymbol{\Omega}$ are omitted for brevity. The plots show that the main diagonal of the MAC matrix equals one, as expected. In contrast, some off-diagonal terms indicate that certain modes in $\boldsymbol{\Psi}_{\mathrm{U_{LR}}}$ are highly correlated and may thus be discarded based on a threshold τ. For instance, the 31st mode shows strong correlation with the first one (MAC $\geqslant$ 0.8) and can potentially be eliminated from the basis (cf. Fig. 6(b)). Conversely, the second, third, and fourth modes do not exhibit high similarity with any other ones, being retained during MOR. This procedure iterates until all eigenvectors in $\boldsymbol{\Psi}_{\mathrm{U_{LR}}}$ have been checked, ensuring an improved basis is obtained.

Fig. 7 thus shows structural and acoustic FRFs computed by the WFEM for the configuration illustrated in Fig. 3, assuming $n_{\mathrm{CB}} = 5$, $n_{\text{L-CC}_\mathrm{I}} = 5$, $n_{\text{L-CC}_\mathrm{B}} = 2$, and varying τ, along with reference solutions. The results reveal that the FRFs are almost unaffected by τ, although the number of boundary DoFs decreases from 117 to 73 as τ changes

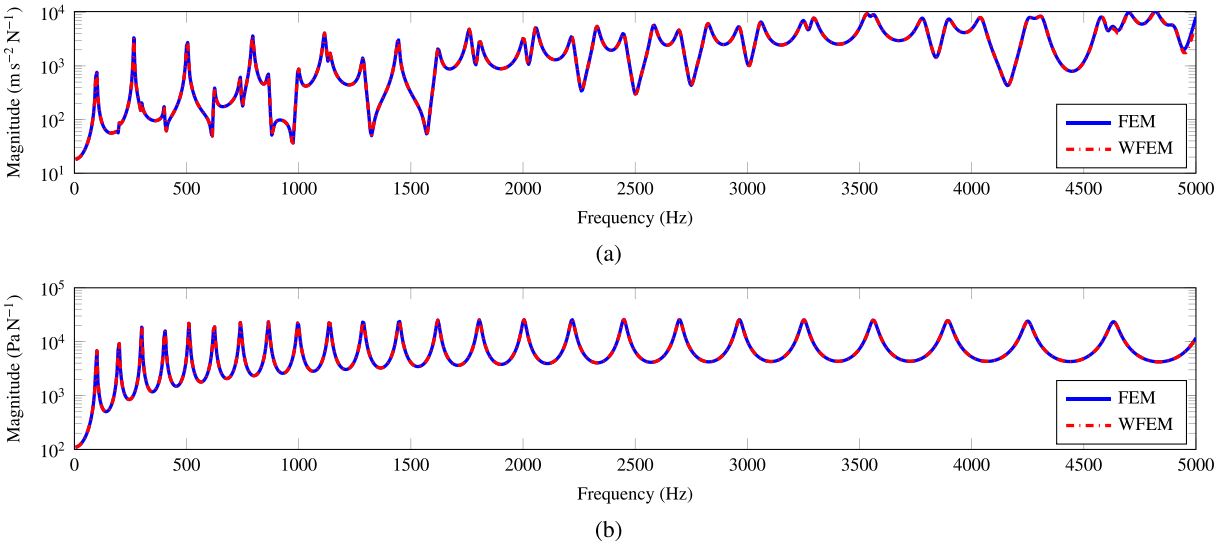

Fig. 4. Magnitude of a) accelerance and b) pressure FRFs calculated for the finite acousto-elastic system shown in Fig. 3 using the FEM and WFEM. For the WFEM, calculations were performed using a unit cell reduced-order model, with only uncoupled internal DoFs reduced through the CB method ($n_{\mathrm{CB}} = 5$).

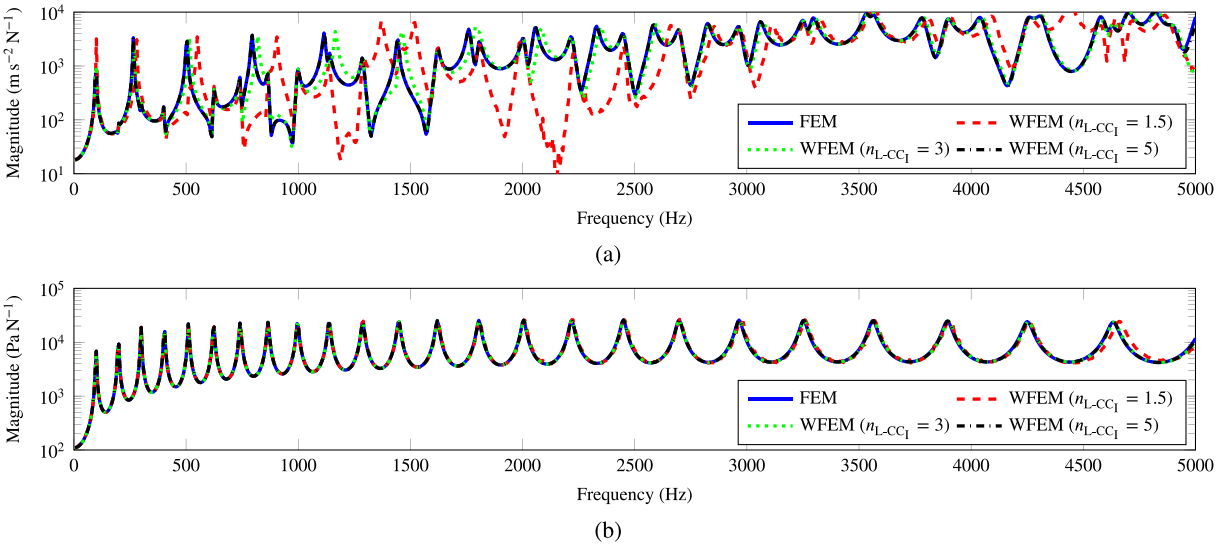

Fig. 5. Magnitude of a) accelerance and b) pressure FRFs calculated for the finite acousto-elastic system shown in Fig. 3 using the FEM and WFEM. For the WFEM, calculations were performed using a unit cell reduced-order model, with uncoupled internal DoFs reduced using the CB method ($n_{\text{CB}} = 5$), and coupled internal DoFs reduced using L-CC.

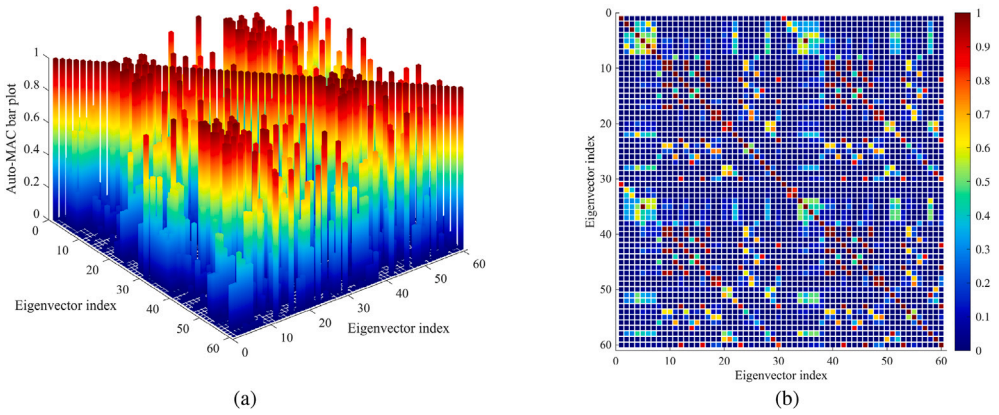

Fig. 6. Auto-MAC of $\boldsymbol{\Psi}_{\text{U}_{\text{LR}}}$: a) three-dimensional bar plot and b) matrix-heatmap.

from 1 to 0.7. Hence, τ can be set lower than 1 to i) keep the model size small; ii) limit the number of wave modes available for computations; and iii) mitigate numerical issues—although this latter point is not critical here, it often arises within the WFEM and can be efficiently addressed by MAC-based filtering, cf. [17] and Appendix A.2. Fig. 7 also indicates that the pressure response is less sensitive to DoF reduction, as seen earlier in Fig. 5. Additionally, the zoomed plot shows that the reduced-order models are slightly stiffer than the reference one, with small amplitude deviations, due to the truncation of higher-order modes by the MOR strategy. It should be noted, however, that these discrepancies stem not only from the reduction of boundary DoFs but also from the reduction of interior DoFs. According to this discussion, τ is set to 0.8 for the remainder of this work, unless otherwise specified.

To summarize, parametric analyses were conducted to assess the influence of key parameters on the proposed MOR procedure when it is applied to a simple, straight acousto-elastic unit cell, through the computation of FRFs for a structure composed of $N = 6$ cells. The values $n_{\text{CB}} = 5$, $n_{\text{L-CC}_\text{I}} = 5$, $n_{\text{L-CC}_\text{B}} = 2$, and $\tau = 0.8$ were selected as they rendered a good compromise between accuracy and model size. In cases where no eigenvalue is found within the band defined by $n_j f_{\max}$, for $j \in \{\text{CB, L-CC}_\text{I}, \text{L-CC}_\text{B}\}$, a single mode is retained in the corresponding basis. On the other hand, if the count of modal DoFs in a basis exceeds the corresponding number of physical DoFs associated with a particular set of equations, the respective projection matrix is discarded and replaced by an identity matrix, meaning no reduction is applied to that DoF set.

4.1.4. Calculation of acousto-elastic dispersion curves, wave modes, and harmonic deformation patterns

After suitable values for the user-defined parameters related to the MOR have been determined, the accuracy of reduced-order models in computing acousto-elastic i) dispersion curves, ii) wave shapes, and iii) harmonic deformation patterns is assessed, in accordance with step **(5)** in Fig. 1. It should be explained that these outputs are only examined for this simpler, introductory example, which adopts a coarser mesh for the considered unit cell, because full-order model simulations are taken as reference solutions—something that showed impractical for the cases addressed next, which employ converged meshes and therefore exhibit many DoFs per cell; and taking into account the hardware used for computations (DELL XPS 8920 desktop with an Intel(R) Core(TM) i7-7700 CPU and 32.0 GB RAM).

Accordingly, Bloch wavenumbers for an infinite acousto-elastic waveguide are calculated as $k_j = \ln(\mu_j)/(-i\Delta)$, with the first five shown

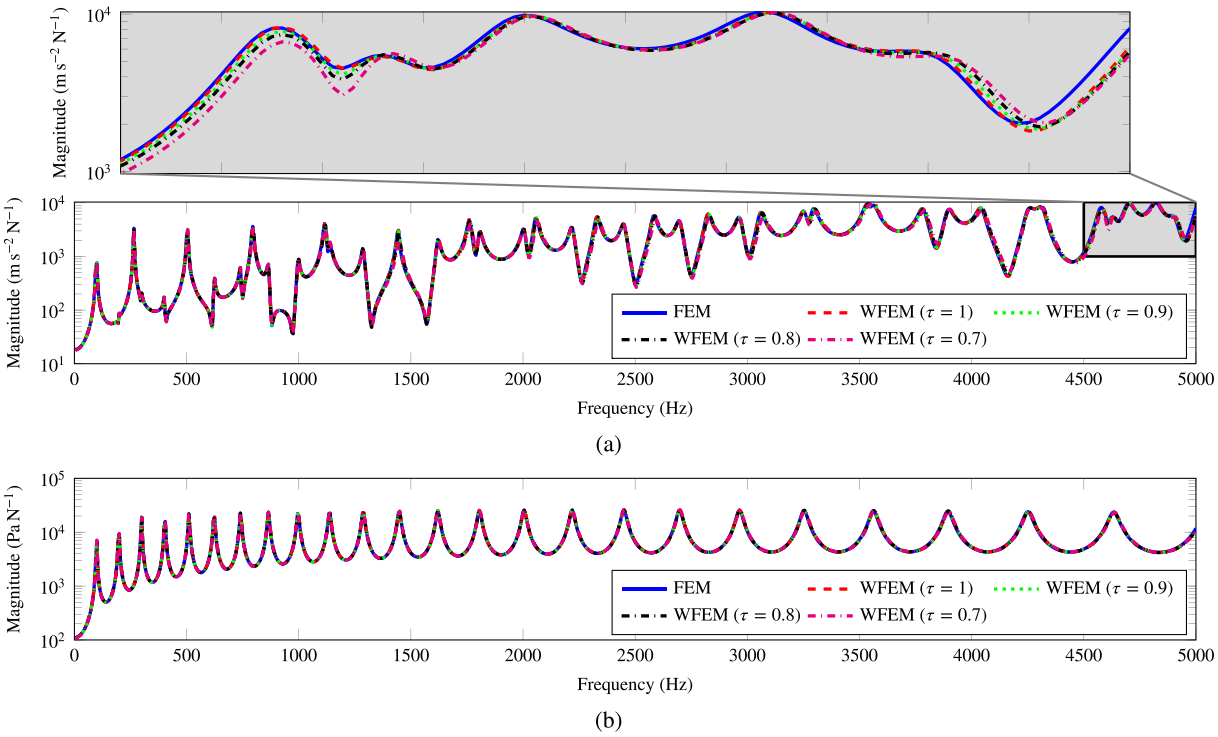

Fig. 7. Magnitude of a) accelerance and b) pressure FRFs calculated for the finite acousto-elastic system shown in Fig. 3 using the FEM and WFEM. For the WFEM, calculations were performed using a unit cell reduced-order model, with uncoupled internal DoFs reduced using the CB method ($n_{\text{CB}} = 5$), and coupled internal and boundary DoFs reduced using L-CC ($n_{\text{L-CC}_\text{I}} = 5$ and $n_{\text{L-CC}_\text{B}} = 2$).

in Fig. 8, considering both full and reduced-order unit cell FE models, along with their maximum relative difference (MRD) measures [62]. The results demonstrate the accuracy of the reduced model, as dispersion curves match closely, with MRDs mostly below 1%. Peaks in Re $\{k_j\}$ MRDs near 1500 Hz, 2900 Hz, and 4750 Hz arise from folds in the dispersion curves due to Bloch wavenumbers being restricted to the irreducible Brillouin zone. Notice that the imaginary part of the wavenumbers are non-null due to the consideration of hysteretic structural damping in the unit cell model.

Besides Bloch wavenumbers, wave modes are often of interest, as they depict the shape of waves traveling through the lattice. Wave modes computed using full- and reduced-order models for the wavenumbers featuring solid-circle markers in Fig. 8, at a frequency of 500 Hz, are shown in Fig. 9, considering $N = 10$ for better visualization. As one

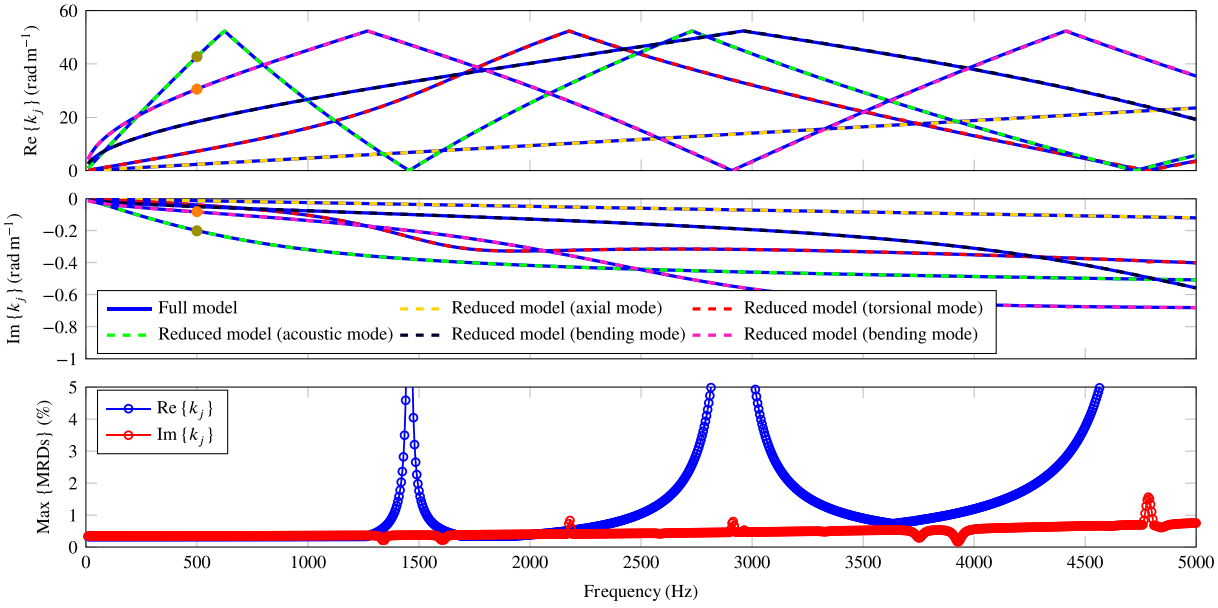

Fig. 8. Dispersion curves for an infinite acousto-elastic waveguide with unit cells in Fig. 3 and their MRD measures. The filled circular markers identify wavenumbers for which wave modes are shown in Fig. 9.

may notice, all wave shapes computed using the reduced-order model are in excellent agreement with the reference results from the full-order model, as confirmed by MAC values above 0.99. In Fig. 9(a), the wave mode exhibits bending behavior in the XY-plane (cf. Fig. 3 for axes orientation), whereas it is mostly associated with acoustic waves in Fig. 9(b) (note that plane waves travel through the fluid domain). In both cases, the fluid and structural dynamics are coupled through the FSI, and therefore elastic waves can excite the fluid medium and vice versa.

Another result of potential interest corresponds to harmonic deformation patterns, as depicted in Fig. 10 for the first acousto-elastic coupled mode in Fig. 7, at 100 Hz, considering the input force being applied at the location indicated in Fig. 3 ($N = 6$). As one may observe, the deformation patterns from the reduced-order model closely match the reference results, with their MAC numbers exceeding 0.99. This, together with previous results, cf. Fig. 7, indicates that the reduced model can predict the dynamic behavior of the acousto-elastic waveguide both locally, via FRFs, as well as globally. At 100 Hz, the structure exhibits bending in the XY-plane (cf. Fig. 3 for axes orientation), resembling the first vibration mode of a homogeneous beam with free-free BCs, which induces pressure variations in the fluid. In turn, the structure-induced pressures excite the structural domain as well, due to the coupled dynamics between both media. In fact, the harmonic deformation patterns presented in Fig. 10, together with the FRFs in Fig. 7, elucidate the so-called strong fluid–structure interaction referred to throughout this work. Since the structure is compliant and the fluid is "heavy", acousto-elastic responses influence each other. Indeed, sharp peaks can be observed at 100 Hz in Fig. 7, simultaneously in the accelerance and pressure FRFs, the corresponding deformed shapes being shown in Fig. 10. The coupled nature of structural and fluid responses at this and other resonance frequencies clearly ensues due to the two-way interaction between both media—which ultimately allows for strong interactions, depending on coupling strength. Similar behavior, or perhaps stronger interactions between fluid and structural domains would likely occur in acousto-elastic periodic structures involving thinner walls and/or heavier fluids. Whilst the consideration of numerous cases, related to different coupling strengths, lies beyond the scope of this work, complementary examples considering the application of the novel GBMS and WFEM to acousto-elastic periodic structures with a heavier fluid and other unit cell geometries are provided in Appendix A for interested readers.

4.2. Straight waveguide with high-order unit cell finite element model

The same straight waveguide addressed in Subsection Section 4.1 is reconsidered here, but now using a mesh with many more DoFs, with two elements through the thickness of PLA, an element size (ES) of 2 mm, and FEs with quadratic interpolation functions (cf. Fig. 11 versus Fig. 3). This mesh was selected based on a convergence analysis of the largest natural frequency of the unit cell subjected to free-free BCs, lying between 0 and $f_{\max}$ and associated with the same eigenvector. The corresponding results are presented in Table 1, which shows that good convergence is achieved with ES = 2 mm, though improved accuracy could be obtained with a smaller ES. Despite the fact that the investigated system can be understood as quite simple, both geometrically and material-wise, with this mesh refinement one aims to address issues which can arise when dealing with systems that require finer spatial resolution, due to the maximum frequency of interest being high. The finite structure still has $N = 6$ unit cells, as in Fig. 3.

Following steps **(1)–(4)** in Fig. 1, the unit cell equations of motion were obtained and then reduced by using the proposed MOR scheme ($n_{\mathrm{CB}} = 5$, $n_{\text{L-CC}_{\mathrm{I}}} = 5$, $n_{\text{L-CC}_{\mathrm{B}}} = 2$, and $\tau = 0.8$). Table 2 summarizes the number of physical and modal DoFs for each DoF set defined earlier (cf. Fig. 2). Note that 25272 structural ($\hat{\mathbf{q}}_{\mathrm{U_I}}$) and 5027 acoustic ($\hat{\mathbf{q}}_{\mathrm{P_I}}$) interior and uncoupled DoF sets have been reduced to single modal DoFs, as no fixed-interface mode obtained from eigenproblems presented in Eq. (11) has frequency below $n_{\mathrm{CB}} f_{\max} = 25000$ Hz. Also noteworthy in Table 2 is

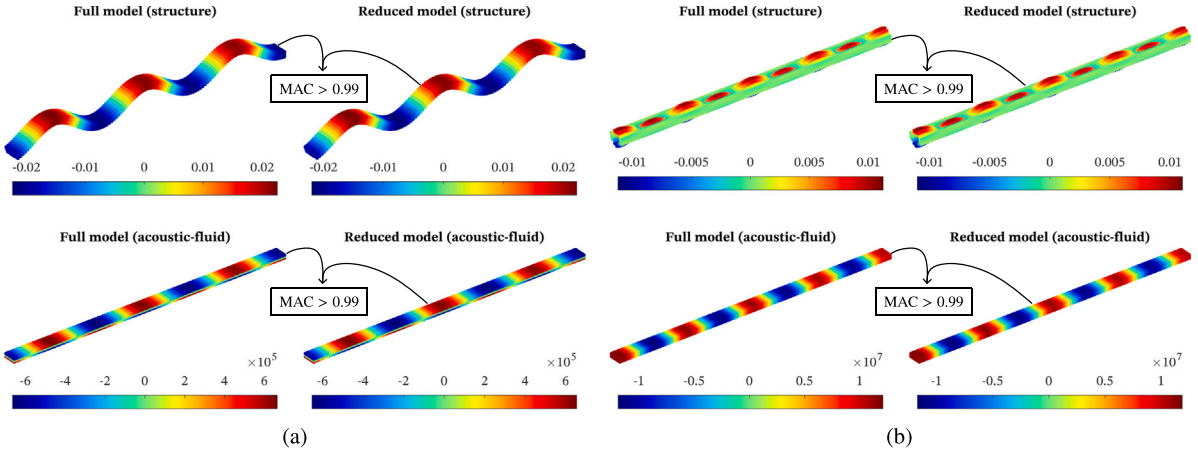

Fig. 9. Wave modes corresponding to wavenumbers featuring a) orange and b) olive markers in Fig. 8, at 500 Hz, computed using full- and reduced-order unit cell FE models. Colormaps represent displacements along the Y-direction (cf. Fig. 3) and pressure.

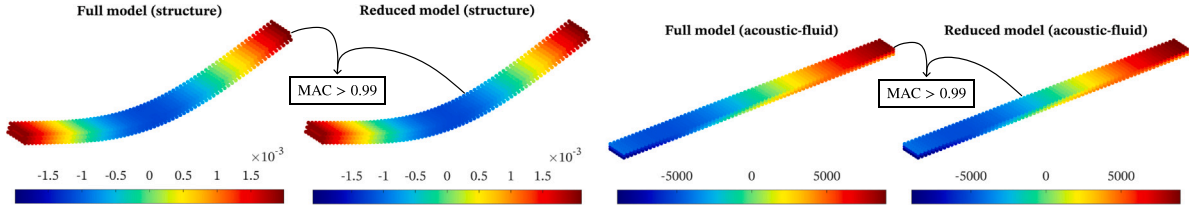

Fig. 10. Harmonic deformation patterns computed for the first acousto-elastic coupled mode in Fig. 7, at 100 Hz, associated with the waveguide shown in Fig. 3, using full- and reduced-order unit cell FE models. Colormaps represent displacements (mm) along the Y-direction (cf. Fig. 3) and pressure (Pa).

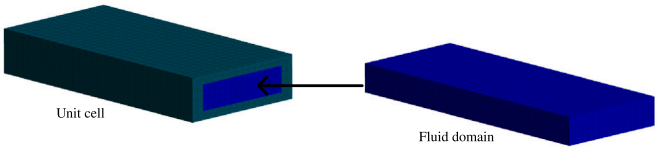

Fig. 11. Unit cell finite element mesh considering quadratic interpolation functions and smaller element size.

Table 1
Convergence analysis of the largest natural frequency of the unit cell shown in Fig. 11 that lies between 0 and $f_{\max}$ and is associated with the same eigenvector.

ES (mm)	Natural frequency (Hz)	RE (%)
4.0	5085.0	–
2.0	4881.1	4.18
1.0	4855.7	0.52

the significant reduction of internal FSI DoFs, from 12672 to 376. In total, 45109 DoFs are decreased to 726, which corresponds to a reduction of 98.4%.

It should be highlighted that one of the features that contributes the most to the drastic reduction of the structural and acoustic uncoupled DoF sets ($\hat{\mathbf{q}}_{\mathrm{U_I}}$ and $\hat{\mathbf{q}}_{\mathrm{P_I}}$, respectively) corresponds to the unit cell's left and right boundaries, as well as the FSIs, being constrained during step **(2)**, rendering the resulting models stiffer. As only one fixed-interface mode is required for each of these sets of DoFs, it would be logical to describe their physical domain with fewer elements, given their "quasi-static" behavior. However, note that the mesh refinement considered for the unit cell was determined through the convergence analysis presented in Table 1, which ensured that the largest natural frequency lying between 0 and $f_{\max}$, considering free-free BCs, is reasonably predicted. Also observe that, although only one fixed-interface mode is included in $\boldsymbol{\Xi}_{\mathrm{U_I}}$ and another one in $\boldsymbol{\Xi}_{\mathrm{P_I}}$, 376 eigenvectors span $\boldsymbol{\Psi}_{\Gamma_{\mathrm{I}}}$, which further justifies the need for a reasonably fine mesh for proper description of the unit cell interior. Beyond resorting to the reduction of Δ, which is not always possible, cf. previous discussions, the number of internal DoFs of the unit cell probably can also be reduced by the use of a nonuniform mesh, with local refinement at FSIs, for example. This latter option, on the other hand, can complicate the meshing process and may be problematic, as highly distorted FEs could be created, thereby deteriorating mesh quality and compromising the accuracy of results.

After these remarks, Fig. 12 shows FRFs obtained using the FEM and WFEM, based on the unit cell FE mesh portrayed in Fig. 11 and for the input/output locations presented in Fig. 3 ($N = 6$). It also includes plots for error assessment, of the RE between FRF resonances and the Cross Signature Scale Factor (CSF) [63]. As one may notice, the FRFs computed with the reduced-order model and WFEM are in very good agreement with the reference solutions obtained via FEM with full-order model. The REs between FRF resonances do not exceed 1.5%, mostly lying below 1%, and the CSFs remain very close to 1. In addition, REs and CSFs indicate that the pressure response is more accurate than the structural one, as observed previously in Subsections Sections 4.1.2 and 4.1.3. To improve the accuracy of structural responses obtained by the reduced-order model, if needed, one could: i) consider the effect of residual modes in the MOR steps described earlier; or ii) increase n_{CB}, $n_{\mathrm{L\text{-}CC_I}}$, $n_{\mathrm{L\text{-}CC_B}}$, and τ values. It should be noted, however, that these strategies may increase computational cost and strategy ii) could lead to numerical issues within the WFEM [17].

Table 3 summarizes the timing data for computing the FRFs shown in Fig. 12. Simulations were performed on a DELL XPS 8920 desktop with an Intel(R) Core(TM) i7-7700 CPU and 32.0 GB RAM, with all codes implemented in MATLAB®. The data show that most of computational time needed to obtain the FRFs using the WFEM is related to the reduction of $\hat{\mathbf{q}}_{\mathrm{U_I}}$ and $\hat{\mathbf{q}}_{\mathrm{P_I}}$ DoFs, step **(2)** in Fig. 1, due to the calculation of fixed-interface modes from eigenproblems presented in Eq. (11), constraint modes from Eq. (13), and matrices appearing in Eq. (14). To speed up these operations, one could, for instance, resort to algebraic condensation [27]. The reduction of $\hat{\mathbf{q}}_{\Gamma_{\mathrm{I}}}$ DoFs, step **(3)**, is the second most computationally intensive task reported in Table 3, though it is approximately five times less demanding than the reduction of interior, uncoupled DoFs, due to the smaller number of equations related to the first set. The time required for this step is related to the solution of the eigenvalue problems given in Eqs. (19) and (20), as well as computation of matrices seen in Eq. (24). The computation of wave modes and frequency tracking of propagation constants (the latter being not necessary to obtain forced responses) ranks third. The remaining tasks listed in Table 3 require negligible computational time in comparison to the aforementioned ones.

Table 3 also shows that the WFEM is more than two times faster than traditional FEM, in terms of wall-clock time. Naturally, as the number of unit cells of a finite periodic structure increases, the WFEM efficiency becomes even more pronounced due to its superior capability to handle large-scale periodic structures (recall that the WFEM requires meshing only a single unit cell of the lattice to perform simulations). For example, if N would be taken equal to 20, then the WFEM would be almost 10 times faster than the traditional FEM, as revealed by numerical experiments not shown here for brevity. Note that, for the specific system investigated in this section, computations with the WFEM could certainly be sped-up by shortening the unit cell length Δ, as it comprises a straight waveguide. This strategy, nevertheless, is not always available, e.g., when the unit cell of interest shows one or multiple geometric features that prevent one from shortening it, as considered in the sequence.

5. Application of the novel GBMS and the WFEM to acousto-elastic periodic structures

In this section, more complex examples are addressed, involving unit cells that have not only many DoFs, finer meshes, and FEs with quadratic interpolation functions, but also featuring a length Δ that cannot be deliberately reduced, incurring in a reduction of the number of internal DoFs, as could have been done in the examples shown previously. In the cases now considered, MOR becomes of utmost importance; otherwise, large-size unit cell FE models would compromise the WFEM performance, making its application quite challenging or even impossible. First, a periodic structure with confined fluid is considered in Section 5.1, with both numerical verification and experimental validation being provided. Then, a similar system is addressed in Section 5.2, but with the unit cell translated by $\Delta/2$, such that the fluid occupies both its interior and its boundaries. In both cases, the fluid is once again taken to be water. To comprehensively demonstrate the applicability of the modeling framework introduced in this work, it should be recalled that additional examples are provided in Appendix A, considering a heavier fluid (mercury), asymmetric unit cell geometries, and thinner walls.

5.1. Acousto-elastic periodic structure with fluid confined within unit cells

The "true" periodic structure considered now is an acousto-elastic system with rectangular cuboid unit cells measuring 60 mm × 10 mm × 30 mm (Δ = 60 mm), featuring a perfectly centered cavity of 53.6 mm × 6 mm × 23.6 mm [55]. The finite system has $N = 6$ unit cells and was manufactured via fused-filament deposition using PLA, as shown in Fig. 13(a). Fabrication was done in two parts to allow cavities to be filled, i.e., a base (Fig. 13(b)) and a closing cap (Fig. 13(c)) were manufactured separately. Prior to filling, the internal voids and the cap were sealed with a thin coat of varnish to prevent leakage. Each cavity was then completely filled with water, and the cap was bonded to the base, yielding the assembly shown in Fig. 13(d) (the water-filled cavities not being visible because the material is opaque).

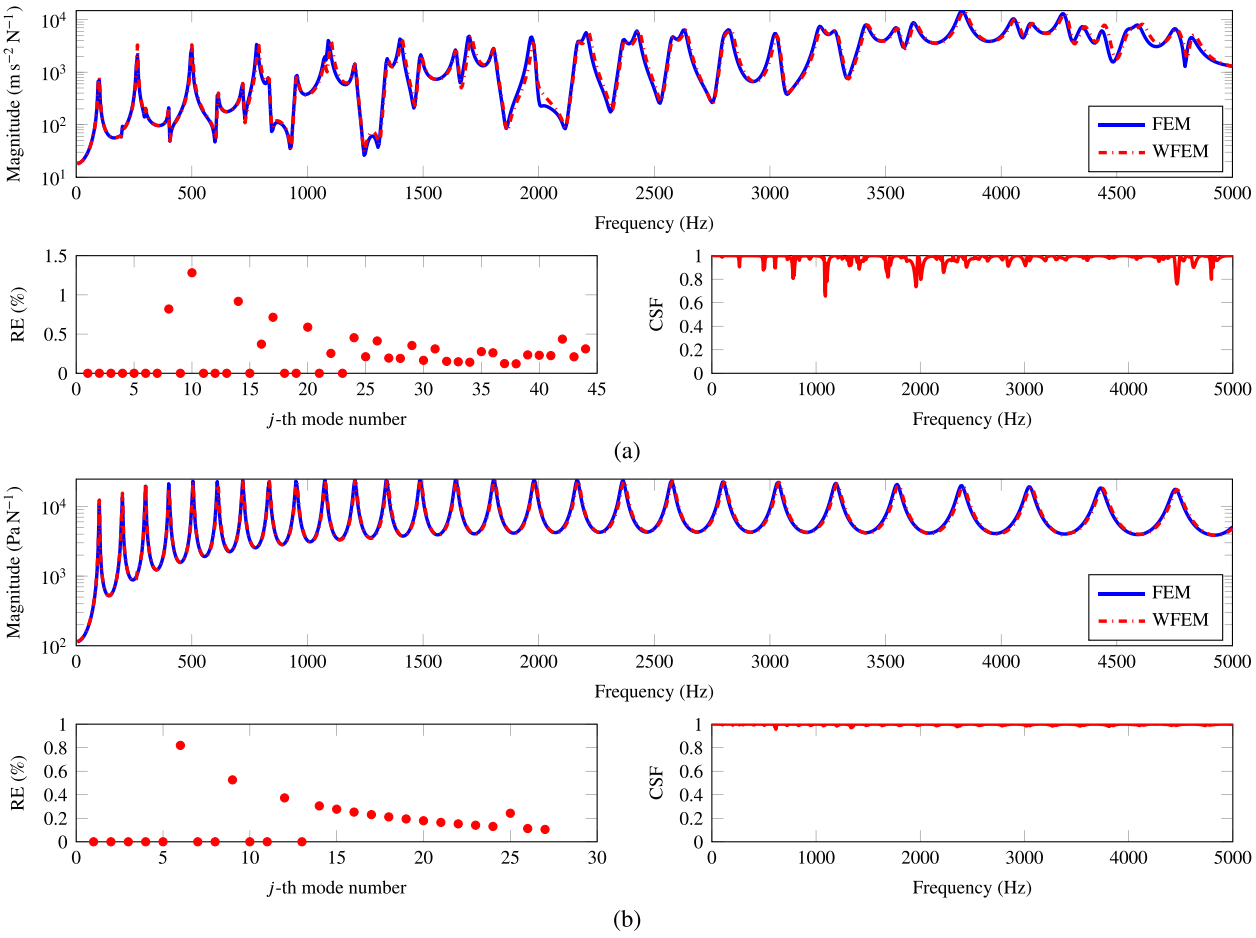

Fig. 12. Magnitude of a) accelerance and b) pressure FRFs for a finite acousto-elastic waveguide, as shown in Fig. 3 but considering the unit cell mesh presented in Fig. 11, computed using the FEM and WFEM, along with the corresponding REs and CSFs. For the WFEM, a reduced-order unit cell model was employed, with $n_{\mathrm{CB}} = 5$, $n_{\mathrm{L\text{-}CC_I}} = 5$, $n_{\mathrm{L\text{-}CC_B}} = 2$, and $\tau = 0.8$.

Following step **(1)** in Fig. 1, an FE model for a unit cell of the lattice was generated, assuming linear, isotropic material behavior and employing FEs with quadratic interpolation functions, having a size of 2 mm (Fig. 14). This mesh was selected based on the convergence of the largest natural frequency of the unit cell, limited to $f_{\max}$, subjected to free-free BCs, following the same procedure adopted previously in Section 4.2. The corresponding results are reported in Table 4, which shows that the natural frequency associated with the target eigenvector does not vary significantly when the ES decreases from 2.0 mm to 1.0 mm, as the RE stays slightly above 2%. Although a better convergence could

Table 2
Number of physical and modal DoFs for the unit cell FE model shown in Fig. 11.

	Set of DoFs									
	U_L	P_L	Γ_L	U_R	P_R	Γ_R	U_I	P_I	Γ_I	Total
Full-order model	648	133	288	648	133	288	25272	5027	12672	45109
Reduced-order model ($n_{\mathrm{CB}} = 5$, $n_{\mathrm{L\text{-}CC_I}} = 5$, $n_{\mathrm{L\text{-}CC_B}} = 2$, and $\tau = 0.8$)	44	36	94	44	36	94	1	1	376	726

Table 3
Timing data (wall-clock time), in seconds, related to the calculation of the FRFs depicted in Fig. 12.

Task	Related equations	WFEM	FEM
Reduction of uncoupled internal DoFs	(8)–(14)	5523	–
Reduction of coupled internal DoFs located at the FSI	(15)–(24)	1043	–
Reduction of boundary DoFs	(20), (25)–(31)	92	–
Computation of wave modes and frequency tracking of propagation constants	(38)	317	–
Calculation of **Q** and **Q***	–	145	–
Evaluation of physical responses	(39), (40), (33)–(35)	17	17051
Other (import of FE data, conditioning of matrices, creation of figures, etc.)	(1)–(7)	124	–
Total	–	7261	17051

Fig. 13. Manufacturing and parts making up the tested acousto-elastic periodic structure: a) fused-filament deposition manufacturing; b) base; c) closing cap; and d) final assembled structure with unit cells fully-filled with water.

be achieved by meshing the unit cell with smaller FEs, computer memory constraints have limited such a task—note, later, in Table 5, that the unit cell model size considered here is larger than that employed previously in Section 4.2 (cf. Table 2), exceeding 50000 equations.

The same n_{CB}, $n_{\mathrm{L\text{-}CC_I}}$, $n_{\mathrm{L\text{-}CC_B}}$, τ, and material properties introduced earlier are considered again for simulations, with the exception of the damping model, which now relies on the Rayleigh coefficients $\alpha = 26.35\,\mathrm{s}^{-1}$ and $\beta = 1.72 \times 10^{-6}$ s. These have been identified from experimental data, considering modal parameters extracted using Polymax [64]. In this setting, Eq. (37) is replaced by:

$$\left(-\omega^2 \begin{bmatrix} \mathbf{M}_{\mathrm{U}} & \mathbf{0} \\ \mathbf{0} & -\rho\mathbf{M}_{\mathrm{P}} \end{bmatrix} + \mathrm{i}\omega \begin{bmatrix} \alpha\mathbf{M}_{\mathrm{U}} + \beta\mathbf{K}_{\mathrm{U}} & \rho\mathbf{R} \\ \rho\mathbf{R}^{\mathrm{T}} & -\alpha\rho\mathbf{M}_{\mathrm{P}} - \beta\rho\mathbf{K}_{\mathrm{P}} \end{bmatrix} + \begin{bmatrix} \mathbf{K}_{\mathrm{U}} & \mathbf{0} \\ \mathbf{0} & -\rho\mathbf{K}_{\mathrm{P}} \end{bmatrix}\right) \begin{Bmatrix} \mathbf{Q}_{\mathrm{U}} \\ \mathbf{Q}_{\varphi} \end{Bmatrix} = \begin{Bmatrix} \mathbf{F}_{\mathrm{U}} \\ \mathbf{F}_{\varphi} \end{Bmatrix}. \tag{41}$$

Table 5 then summarizes the number of DoFs before and after reducing the unit cell FE model, where $\mathrm{U_I}$ and $\mathrm{P_I}$ DoF sets were again reduced to single structural and acoustic DoFs, with frequencies about 10 and 26 times larger than $f_{\max}$, respectively. Additionally, the number of DoFs in the Γ_{I} DoF set dropped from 14120 to 334, while 2046 boundary DoFs were replaced by just 52 modal ones. The data in Table 5 also indicate that the proposed MOR strategy can reduce 99.3% of the unit cell physical DoFs.

Bending-dominated FRFs were then determined for the manufactured periodic structure with confined fluid considering the setup provided on the left side of Fig. 15, using an impact hammer. Such FRFs can be seen on the right side of the same figure. The results reveal that the FRF computed using the WFEM closely matches the FEM prediction, with REs < 0.7% and CSFs > 0.98 (plots being omitted here for brevity). In addition, the numerical models fairly capture several features of the experimental response, such as resonance frequencies, damping, pass bands, and stop bands (the latter indicated using gray shading in Fig. 15, determined for the corresponding infinite periodic structure, considering the Bloch–Floquet theorem). The discrepancies between the FEM/WFEM and the experimental results displayed in Fig. 15 are attributed to the following points: i) the adoption of a model for the PLA material that does not properly account for viscoelastic behavior [65]; ii) the assumption of isotropic behavior for a structure manufactured via additive manufacturing, and therefore prone to anisotropy [66]; iii) the possibility that some unit cells were not completely filled with fluid, which, in addition to allowing the occurrence of sloshing at the fluid free surface, would alter inertia of the system; and iv) deviations between the nominal geometric dimensions of the periodic model and those of the tested specimen, originating from the manufacturing process. Regarding computational time, the calculation of the reference FRF required approximately 50 days (4320000 s) by the traditional FEM, whereas the WFEM took only 10591 s, showing the WFEM is approximately 410 times faster than the FEM (wall-clock times).

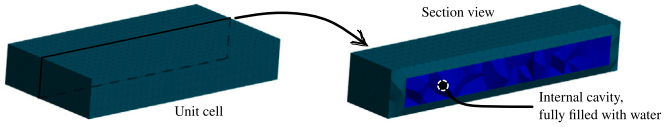

Fig. 14. Finite element mesh of the unit cell of the periodic structure with confined fluid shown in Fig. 13.

Table 4
Convergence analysis of the largest natural frequency of the unit cell shown in Fig. 14 which lies between 0 and $f_{\max}$ and is associated with the same eigenvector.

ES (mm)	Natural frequency (Hz)	RE (%)
4.0	5208.0	–
2.0	4974.7	4.69
1.0	4861.3	2.33

With respect to computational burden, the WFEM showed to be much more efficient than the FEM for the analysis of the acousto-elastic periodic structure presented in Fig. 15. Note that the WFEM involves solving a frequency-dependent linear system of equations to determine $\mathbf{Q}$ and $\mathbf{Q}^*$, whose size corresponds to twice the number of boundary DoFs of the unit cell, whether full or reduced-order models are considered. Thus, in accordance with Table 5, this corresponds to $2 \times 26 = 52$ equations for the problem addressed here. On the other hand, within the FEM, this number increases to 306879, which is almost 3000 times larger than that found for the WFEM. The significantly larger number of equations solved within the FEM is explained by the fact that, in the FEM, i) the full lattice must be discretized to perform dynamic analyses, rather than only a single unit cell as in the WFEM; and ii) FRFs are obtained using the direct method, as the modal superposition method does not yet appear to be available/implemented in the FE software used in this work for acousto-structural dynamic analyses. Besides computational times and problem sizes discussed previously, the WFEM is attractive for the analysis of periodic media because it provides much more than forced responses. This includes, for example, dispersion curves and wave shapes (cf. Figs. Figs. 8 and 9), which can only be derived with traditional FEM (e.g., in COMSOL Multiphysics® software) upon the enforcement of periodic boundary conditions. Such wave-related quantities provide fundamental insight about wave propagation on periodic media and are often indispensable for a complete understanding of their dynamic behavior. Summarizing, the WFEM is probably the best method for the analysis of the periodic structure shown in Fig. 15, as is also the case for examples considered in Section 5.2 and Appendix A.

5.2. Acousto-elastic periodic structure with confined fluid but translated unit cell

Lastly, the unit cell considered in Section 5.1 is analyzed again, but this time with it being translated by $\Delta/2$ along its length, such that

Table 5
Number of physical and modal DoFs for the unit cell FE model shown in Fig. 14.

	Set of DoFs					
	U_L	U_R	U_I	P_I	Γ_I	Total
Full-order model	1023	1023	32193	3640	14120	51999
Reduced-order model ($n_{CB} = 5$, $n_{L\text{-}CC_I} = 5$, $n_{L\text{-}CC_B} = 2$, and $\tau = 0.8$)	26	26	1	1	334	388

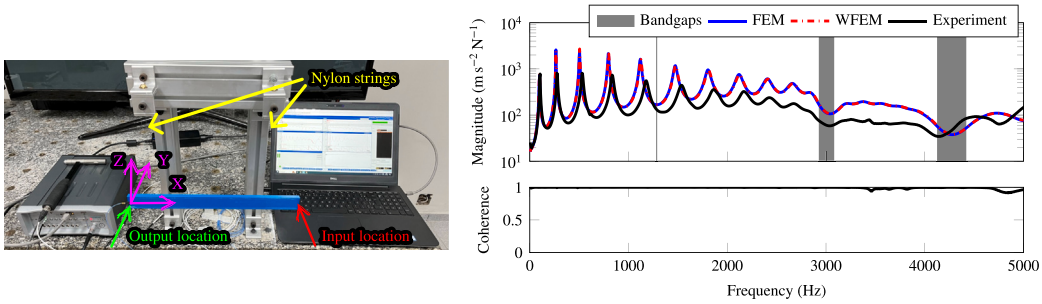

Fig. 15. Experimental setup (left) and bending-related FRFs (right) of the periodic structure with water-filled unit cells.

the boundaries of the resulting geometry end up with both fluid and structural DoFs, as shown in Fig. 16. The same ES adopted in the previous subsection was used for meshing the translated unit cell for the sake of consistency, i.e., ES = 2 mm. With this modified unit cell, one aims to assess whether the novel GBMS combined with the WFEM is suitable to handle such a case, although it leads to an identical infinite structure.

By following steps **(2)–(4)** in Fig. 1, reduced-order models were derived for the unit cell shown in Fig. 16, taking $n_{CB} = 5$, $n_{L\text{-}CC_I} = 5$, $n_{L\text{-}CC_B} = 2$, and $\tau = \{0.8, 0.9, 1\}$. Then, FRFs were computed for a finite periodic structure ($N = 6$) made with such unit cell using the WFEM, considering input/output DoFs just like those indicated in Fig. 3; they are shown in Fig. 17, along with REs and CSFs between FEM and WFEM ($\tau = 1$). The FRFs plotted in Fig. 17 indicate that higher values of τ (> 0.8) are required for WFEM results to perfectly match those obtained with the FEM. In this example, τ strongly affects the number of boundary equations, increasing from 76 when $\tau = 0.8$ to 229 when $\tau = 1$. Since no numerical issues arose in the forced responses, although quite common in the WFEM (cf. [17,61] and Section A.2), the MAC-based mode filtering procedure appears unnecessary and even detrimental to the accuracy of the reduced-order model at high frequency if it is taken as 0.8, and thus $\tau = 1$ shows itself as the simplest and most straightforward choice. Note, however, that other values may also provide accurate reduced-order models, e.g., $\tau \geqslant 0.9$. Accordingly, REs between FRF peaks remain consistently below $\approx 0.6\%$, and CSFs near to 1 in Fig. 17. The depicted FRFs also convey that the fluid response is less sensitive to the proposed MOR strategy, similar to findings reported in Section 4. In terms of wall-clock computational time, the WFEM proved to be twice as fast as the FEM for the case now addressed.

A summary of the number of physical and modal DoFs associated with the unit cell used to obtain the forced responses shown in Fig. 17, for $\tau = 1$, is provided in Table 6, from which it can be appreciated that approximately only 1% of the equations have been retained in the modal model.

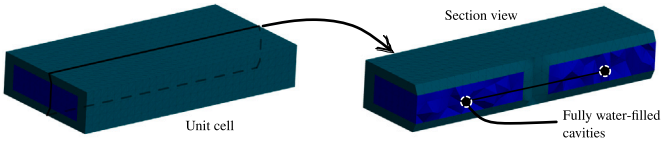

Fig. 16. Finite element mesh of a unit cell of the periodic structure with confined fluid shown in Fig. 13, but considering a translation of $\Delta/2$ along the periodicity direction.

6. Concluding remarks

This work addressed the modeling of acousto-elastic periodic structures involving strong fluid–structure interactions using a novel GBMS strategy together with the WFEM. In the proposed modeling framework, uncoupled structural and acoustic internal DoFs of a unit cell are initially reduced using the CB method, while preserving the FSI and boundary DoFs. Then, internal DoFs related to the FSI are reduced using the L-CC MOR method, employing three sets of Ritz vectors that account for LMs, RBMs, and low-frequency FBMs. Finally, boundary DoFs are reduced using L-CC modes, which take into account three distinct bases during the MOR process and respect conditions necessary to satisfy the Bloch–Floquet theorem. At each step, frequency-based truncation is employed to construct projection matrices, and only right eigenvectors are used during MOR, even though these differ from the corresponding left ones. A MAC-based filtering technique is applied to eliminate almost collinear interface modes, which not only increase the model size but can also lead to numerical issues within the WFEM. Various numerical simulations and an experimental validation have been presented, considering i) straight waveguides; and ii) periodic structures whose unit cell length cannot be freely changed due to material/geometric constraints. The results demonstrated that the proposed MOR scheme yields highly reduced unit cell models, achieving more than 98% reduction in the number of DoFs. These reduced-order unit cell models were then used to compute harmonic forced responses, dispersion curves, wave shapes, and harmonic deformation patterns, all showing excellent agreement with reference results. In terms of computational performance, the WFEM proved to be over four hundred times faster than traditional FEM for the forced response analysis of one of the considered structures. The modeling framework was also validated against experimental data, where bending-related bandgaps of a periodic structure with confined fluid were successfully predicted. This work thus extends the baseline GBMS and WFEM to

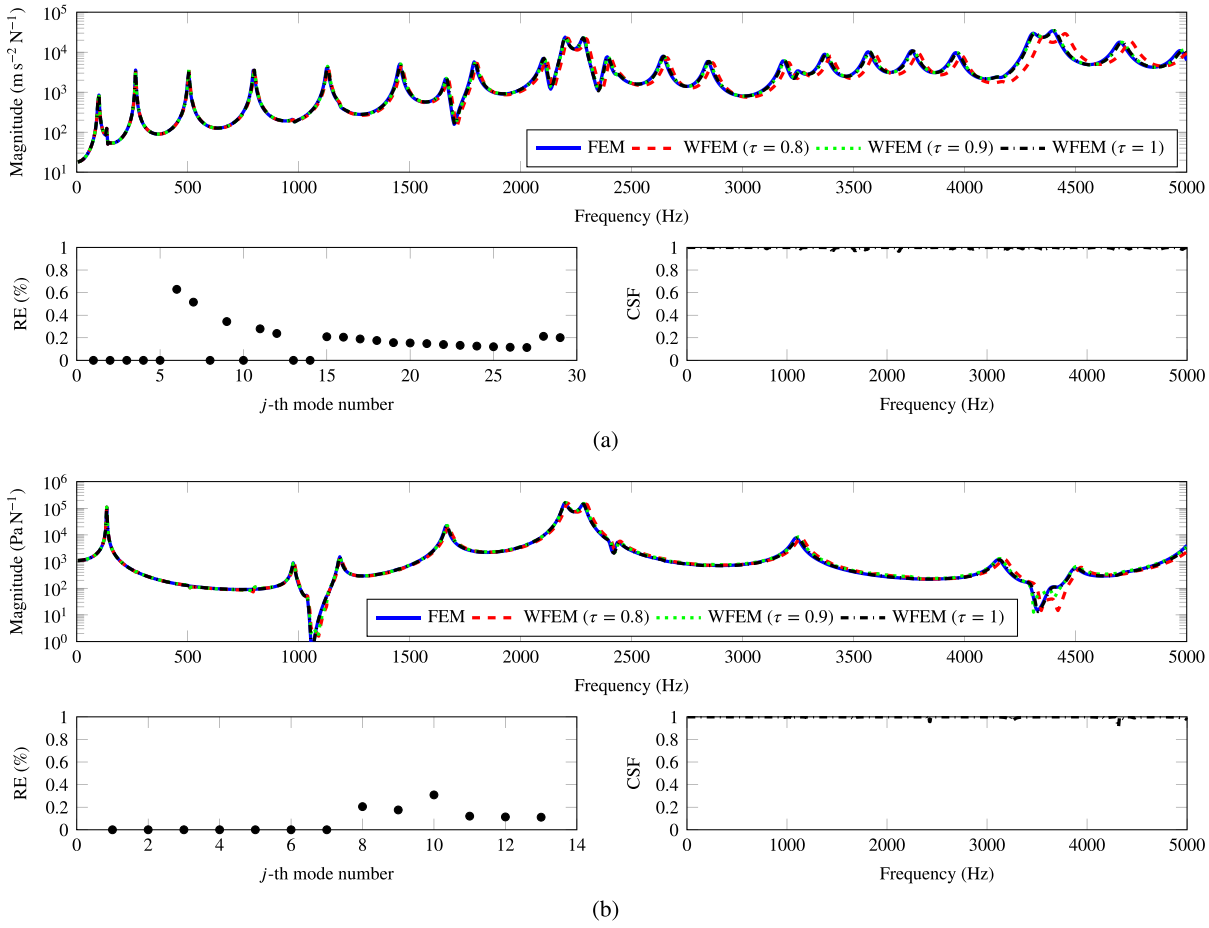

Fig. 17. Magnitude of a) accelerance and b) pressure FRFs calculated for a finite acousto-elastic periodic structure similar to that seen in Fig. 3, but made with unit cells shown in Fig. 16, computed using the FEM and WFEM, along with REs and CSFs between FEM and WFEM ($\tau = 1$) results. For the WFEM, reduced-order unit cell models were employed, with $n_{\text{CB}} = 5$, $n_{\text{L-CC}_\text{I}} = 5$, $n_{\text{L-CC}_\text{B}} = 2$, and $\tau = \{0.8, 0.9, 1\}$.

Table 6
Number of physical and modal DoFs for the unit cell FE model shown in Fig. 16.

	Set of DoFs									
	U_L	P_L	Γ_L	U_R	P_R	Γ_R	U_I	P_I	Γ_I	Total
Full-order model	450	115	240	450	115	240	32904	3813	14360	52687
Reduced-order model ($n_{\text{CB}} = 5$, $n_{\text{L-CC}_\text{I}} = 5$, $n_{\text{L-CC}_\text{B}} = 2$, and $\tau = 1$)	58	51	120	58	51	120	1	2	332	793

the analysis of acousto-elastic periodic structures featuring strong fluid–structure interactions, by means of a MOR strategy that allows for time-efficient and accurate simulations, opening opportunities to explore the analysis, design and/or optimization of acousto-elastic periodic structures.

CRediT authorship contribution statement

Vinícius M. de S. Santos: Writing – review & editing, Writing – original draft, Validation, Methodology, Investigation, Formal analysis, Conceptualization. **Thiago de P. Sales:** Writing – review & editing, Supervision, Resources, Methodology, Investigation, Funding acquisition, Formal analysis, Conceptualization. **Morvan Ouisse:** Writing – review & editing, Supervision, Resources, Methodology, Investigation, Funding acquisition, Formal analysis, Conceptualization.

Declaration of competing interest

The authors declare that they have no known competing financial interests or personal relationships that could have appeared to influence the work reported in this paper.

Acknowledgements

This study was financed, in part, by the São Paulo Research Foundation (FAPESP), Brasil. Process Numbers #2018/15894-0, #2023/11207-7 and #2024/07549-2. This study was financed in part by the Coordenação de Aperfeiçoamento de Pessoal de Nível Superior – Brasil (CAPES) – Finance Code 001. All authors are grateful to FAPESP and CAPES for the financial support of their research activities. M. Ouisse acknowledges the graduate school EIPHI (project ANR-17-EURE-0002).

Appendix A. Application of the novel GBMS with the WFEM to acousto-elastic periodic structures with a heavier fluid, asymmetric unit cells, and thinner walls

This appendix aims to assess the capability of the proposed MOR strategy as applied to unit cells that have been purposely selected, which exhibit stronger coupling strength between fluid and structure subdomains, owing to material and/or geometric characteristics. First, Appendix A.1 considers a unit cell design similar to those analyzed in the main matter of the paper; however, the fluid is assumed to be mercury, exhibiting a density of $13529\,\mathrm{kg\,m^{-3}}$ and a sound speed of $1450\,\mathrm{m\,s^{-1}}$. In addition, the simulated unit cell incorporates communicating channels at its left and right interfaces, which allow the fluid to be present simultaneously in the unit cell interior and at its boundaries. Subsequently, Appendix A.2 addresses a zig-zag-like unit cell which again considers mercury as the fluid medium and exhibits an asymmetric design. Finally, Appendix A.3 presents results related to a unit cell that, besides adopting mercury and being asymmetric, has thinner walls compared to all other considered examples. In all cases, material and/or geometric features do not allow one to shorten the unit cell length, which incurs in models featuring many internal DoFs that can only be analyzed with the WFEM after being reduced.

A.1. Acousto-elastic periodic structure with communicating channels between unit cells

The periodic structure with communicating channels between unit cells addressed here is based on the design presented in Section 5.1 and [55]. Each unit cell therefore has the same dimensions as those reported previously for the model seen in Fig. 14, but additionally incorporates rectangular channels of $4\,\mathrm{mm} \times 16\,\mathrm{mm}$ that extend from its left and right boundaries up to the internal cavity ($3.2\,\mathrm{mm}$ depth). The finite periodic structure is still assumed to have $N = 6$ unit cells. According to step **(1)** in Fig. 1, a single unit cell of the lattice was discretized using FEs, the resulting mesh being presented in Fig. 18. This mesh adopts FEs with quadratic interpolation functions and employs an $\mathrm{ES} = 2.0\,\mathrm{mm}$, both defined with the aim of ensuring model accuracy up to $f_{\max} = 5000\,\mathrm{Hz}$, cf. convergence analysis presented in Table 7 (free-free BCs).

Considering that n_{CB}, $n_{\mathrm{L\text{-}CC_I}}$, $n_{\mathrm{L\text{-}CC_B}}$, and τ are respectively defined as 5, 5, 2, and 0.8, in accordance with Section 4.1, Table 8 shows the number of physical and modal DoFs for each DoF set defined earlier in Fig. 2. As one may notice, 31587 and 3868 physical DoFs are replaced by single structural and acoustic fixed-interface modes in step **(2)**. Moreover, 14880 fluid–structure coupled DoFs Γ_{I} are replaced by 434 generalized coordinates in step **(3)**. Lastly, 2×202 modal DoFs replace 2×1033 physical coordinates associated with the unit cell boundaries. Particularly relevant is the fact that many boundary/interface modes are removed during the MAC-based mode exclusion procedure in step **(4)**, thereby ensuring the unit cell reduced-order model remains smaller, and less prone to numerical issues in the WFEM (results similar to those given in Fig. 6 are not shown for the sake of brevity). Overall, Table 8 shows that 52401 physical DoFs are replaced by 840 generalized coordinates, implying a reduction of 98.4% in the number of equations due to the MOR.

In accordance with step **(5)** in Fig. 1, Fig. 19 shows FRFs obtained using the WFEM, as well as reference FEM results for input/output DoFs as indicated in Fig. 3, together with their REs and CSFs. As can be noticed from Fig. 19, the WFEM solutions closely superpose the reference ones. The REs remain below 0.6% and the CSFs stay very close to 1 for both the structural (Fig. 19(a)) and fluid (Fig. 19(b)) responses.

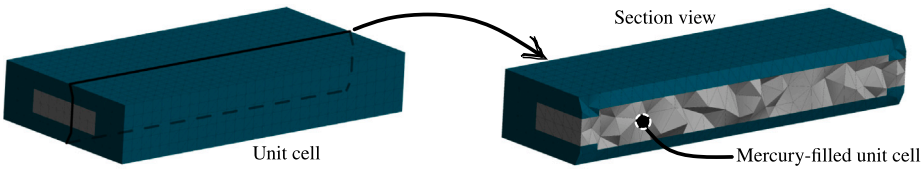

Fig. 18. Finite element mesh and section view of a unit cell of the acousto-elastic periodic structure with communicating channels.

Table 7
Convergence analysis of the largest natural frequency of the unit cell shown in Fig. 18 which lies between 0 and $f_{\max}$ and is associated with the same eigenvector.

ES (mm)	Natural frequency (Hz)	RE (%)
3.0	5135.5	–
2.5	5018.1	2.34
2.0	4975.3	2.03

Table 8
Number of physical and modal DoFs for the unit cell FE model shown in Fig. 18.

	Set of DoFs									
	$\mathrm{U_L}$	$\mathrm{P_L}$	Γ_{L}	$\mathrm{U_R}$	$\mathrm{P_R}$	Γ_{R}	$\mathrm{U_I}$	$\mathrm{P_I}$	Γ_{I}	Total
Full-order model	828	45	160	828	45	160	31587	3868	14880	52401
Reduced-order model ($n_{\mathrm{CB}} = 5$, $n_{\mathrm{L\text{-}CC_I}} = 5$, $n_{\mathrm{L\text{-}CC_B}} = 2$, and $\tau = 0.8$)	70	23	109	70	23	109	1	1	434	840

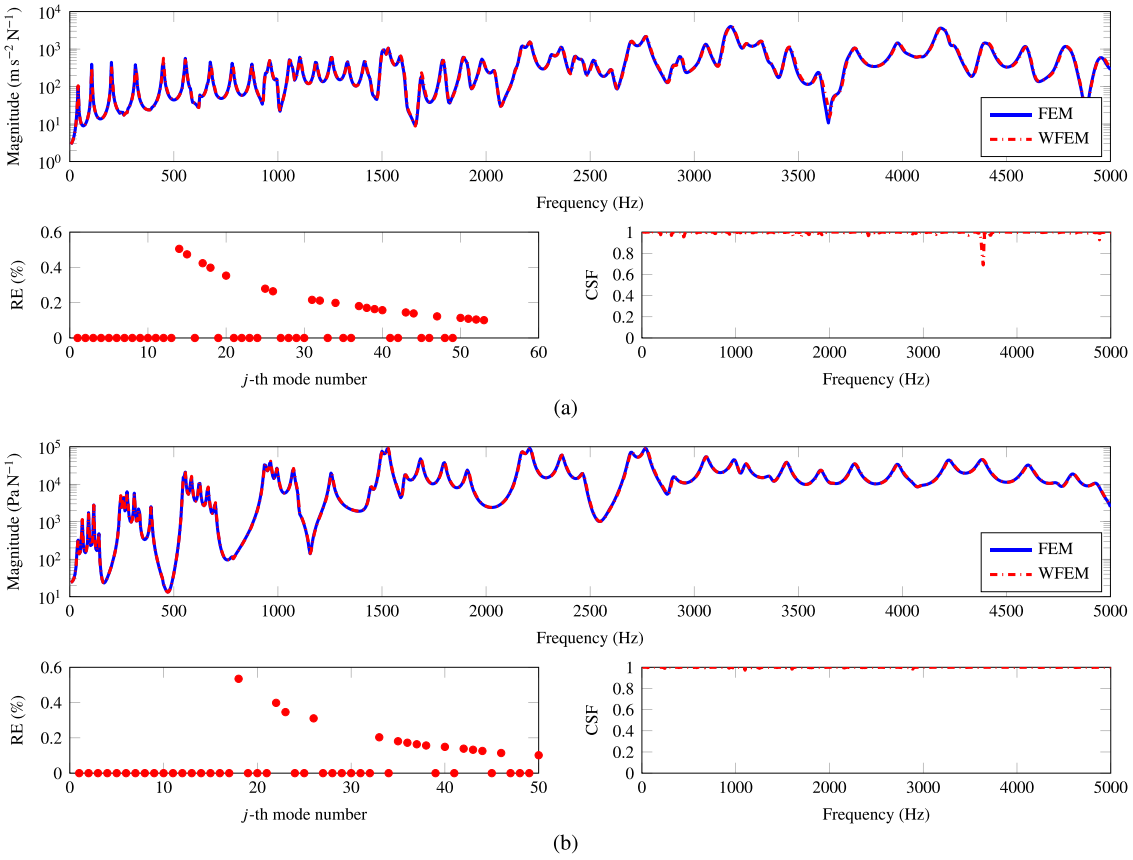

Fig. 19. Magnitude of a) accelerance and b) pressure FRFs for a finite acousto-elastic periodic structure, as shown in Fig. 3 but considering the unit cell model from Fig. 18, computed using the FEM and WFEM, along with the corresponding REs and CSFs. For the WFEM, a reduced-order model was employed, with $n_{\text{CB}} = 5$, $n_{\text{L-CC}_{\text{I}}} = 5$, $n_{\text{L-CC}_{\text{B}}} = 2$, and $\tau = 0.8$.

A.2. Zig-zag-like acousto-elastic periodic structure

A zig-zag-like acousto-elastic periodic structure is now considered, its design being based on [56]. Herein, the zig-zag-like beam incorporates a continuous internal cavity that follows the external geometry of the structure, being perfectly centered within it. The adopted zig-zag-like shape increases the complexity of the unit cell's interior domain, which is interesting for assessing its impact on steps **(2)** and **(3)** of the proposed modeling framework (cf. Fig. 1). In addition, the zig-zag cavity is filled with mercury. Note that the unit cell geometry has been purposely chosen to be asymmetric with respect to the mid-plane between its left and right boundaries (cf. Fig. 20) to better analyze whether the novel GBMS and WFEM are suitable for such condition. For instance, all examples presented so far have focused on unit cell geometries exhibiting symmetry with respect to the aforementioned plane, although symmetric FE meshes have not been guaranteed.

While Fig. 20 presents the geometry and dimensions of the unit cell considered here, Fig. 21 shows the resulting finite zig-zag-like acousto-elastic periodic structure made with $N = 6$ unit cells repeated along the X-direction. Fig. 21 also includes a detailed view of the FE mesh of one unit cell, showing the inner mercury, and input/output DoFs used to obtain FRFs. The unit cell FE model adopts an ES of 2 mm, which, as demonstrated in Table 9, ensures the model's convergence up to f_{max} (for free-free BCs).

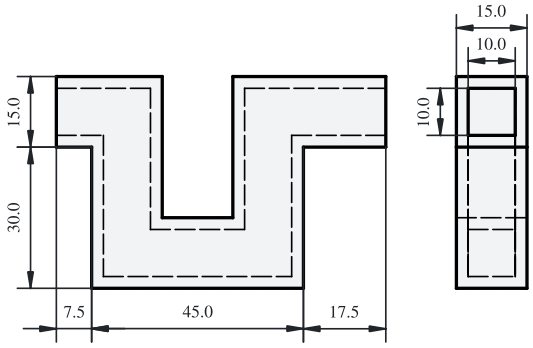

Fig. 20. Geometry and dimensions (mm) of a unit cell used to make a zig-zag-like acousto-elastic periodic structure.

Fig. 22 shows FRFs obtained for the zig-zag-like acousto-elastic periodic structure illustrated in Fig. 21, considering $n_{\mathrm{CB}} = 5$, $n_{\mathrm{L\text{-}CC_I}} = 5$, $n_{\mathrm{L\text{-}CC_B}} = 2$, and $\tau \in \{0.8, 0.7, 0.6\}$. As one may note from the accelerance (Fig. 22(a)) and pressure (Fig. 22(b)) FRFs, minor localized instabilities affect the

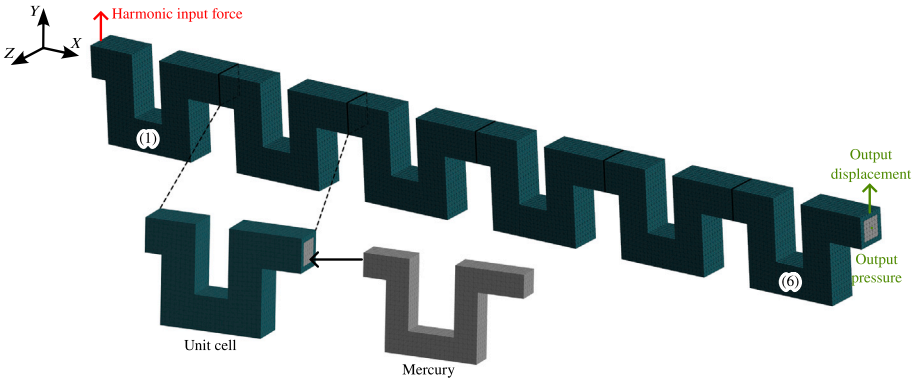

Fig. 21. Finite zig-zag-like acousto-elastic periodic structure with $N = 6$ unit cells, along with the input and output locations considered for calculating the harmonic responses shown subsequently, and a detailed view of a unit cell comprising the structure.

Table 9
Convergence analysis of the largest natural frequency of the unit cell seen in Fig. 21 that lies between 0 and $f_{\max}$ and is associated with the same eigenvector.

ES (mm)	Natural frequency (Hz)	RE (%)
2.5	4997.4	–
2.0	4948.9	0.98
1.5	4907.1	0.85

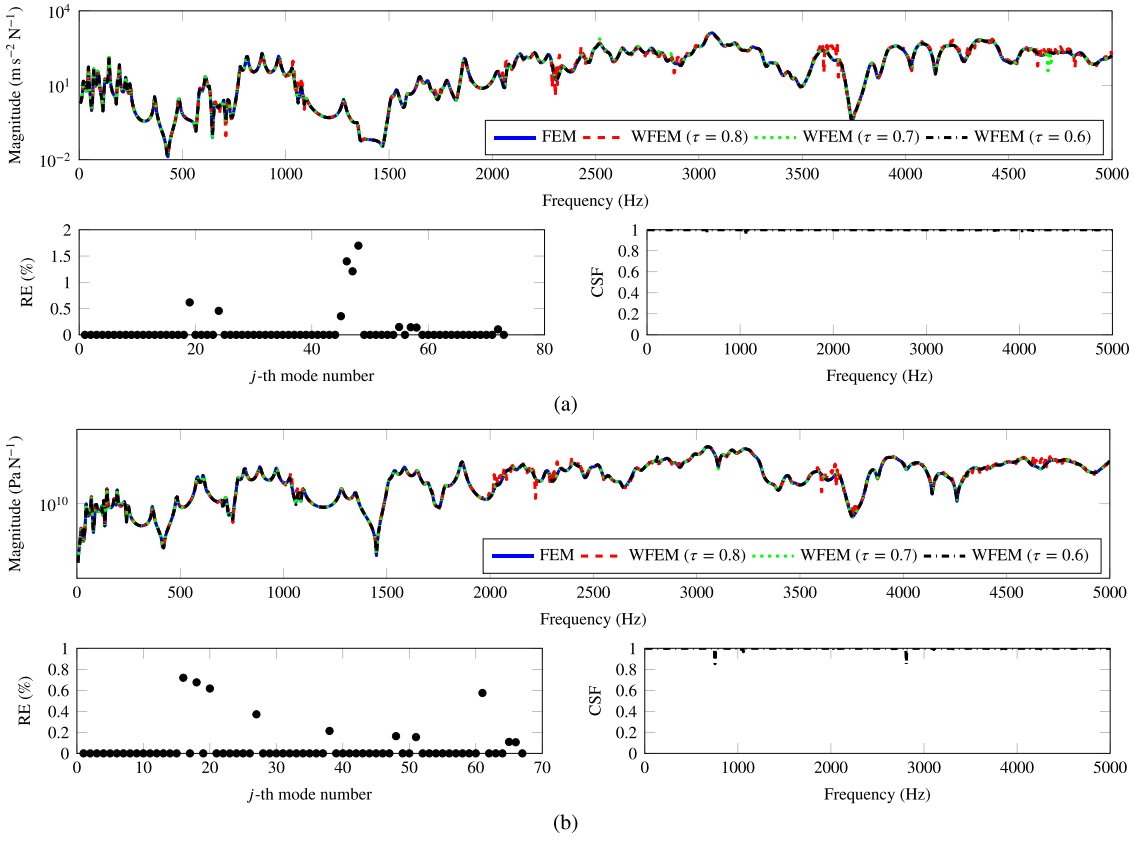

Fig. 22. Magnitude of a) accelerance and b) pressure FRFs calculated for the finite acousto-elastic periodic structure seen in Fig. 21 using the FEM and WFEM, along with the corresponding REs and CSFs ($\tau = 0.6$). For the WFEM, calculations were performed using unit cell reduced-order models, with uncoupled internal DoFs reduced using the CB method ($n_{\mathrm{CB}} = 5$), and coupled internal and boundary DoFs reduced using L-CC ($n_{\mathrm{L\text{-}CC_I}} = 5$ and $n_{\mathrm{L\text{-}CC_B}} = 2$).

accuracy of WFEM responses when $\tau = 0.8$, owing to the large number of wavemodes that are included in the wavemode basis ($\boldsymbol{\Phi}_{\mathrm{Q}}$, $\boldsymbol{\Phi}^{*}_{\mathrm{Q}}$, $\boldsymbol{\Phi}_{\mathrm{F}}$, $\boldsymbol{\Phi}^{*}_{\mathrm{F}}$), some of them poorly computed due to numerical issues, which in total amounts to $2 \times 313 = 626$ left-/right-going waves. These higher-order wavemodes, which impair the WFEM accuracy, can be eliminated by decreasing the threshold value τ used in the proposed MAC-based filtering procedure, which in turn reduces the number of (modal) boundary DoFs of the unit cell, as discussed in [17] for strictly elastic structures—recall that full wavemode bases have always been used in this work to compute forced responses with the WFEM. Fig. 22 therefore shows that significant improvements are obtained when τ takes the value of 0.7 or 0.6. In fact, when $\tau = 0.6$, all numerical instabilities appear to vanish from the WFEM solutions, with the REs and CSFs between WFEM and FEM remaining mostly equal to zero and one, respectively, for both structural and fluid responses. For $\tau = 0.6$, the number of boundary DoFs decreases to 162 (approximately half of those obtained when $\tau = 0.8$), such that the resulting wavemode basis is spanned by $2 \times 162 = 324$ left-/right-going waves, instead of $2 \times 313 = 626$.

Lastly, a summary of the number of physical and modal DoFs for the unit cell FE model seen in Fig. 21 is presented in Table 10. The results show that the uncoupled structural and acoustic internal DoFs are reduced to single fixed-interface modes, whereas a larger number of generalized coordinates replaces the coupled DoFs associated with the Γ_{I} DoF set, in comparison with previous examples. The number of boundary DoFs decreases from 2×589 physical coordinates to 2×162 generalized DoFs ($\tau = 0.6$), yielding a reduction of about 73% in the number of interface DoFs. In total, the number of equations of the full-order physical model drops from 73047 to 1400, indicating that the reduced-order model is 52 times smaller than its physical counterpart.

Table 10
Number of physical and modal DoFs for the unit cell FE model shown in Fig. 21.

	Set of DoFs									
	$\mathrm{U_L}$	$\mathrm{P_L}$	Γ_{L}	$\mathrm{U_R}$	$\mathrm{P_R}$	Γ_{R}	$\mathrm{U_I}$	$\mathrm{P_I}$	Γ_{I}	Total
Full-order model	348	81	160	348	81	160	45981	5248	20640	73047
Reduced-order model ($n_{\mathrm{CB}} = 5$, $n_{\mathrm{L\text{-}CC_I}} = 5$, $n_{\mathrm{L\text{-}CC_B}} = 2$, and $\tau = 0.6$)	53	19	90	53	19	90	1	1	1074	1400

A.3. Acousto-elastic periodic structure with confined fluid, translated unit cell and thinner walls

The last case study examined here is again inspired by the unit cell geometry considered in [55]. However, this time the fluid is taken to be mercury, the unit cell is purposely chosen to be asymmetric with respect to the direction of wave propagation, and it incorporates walls of smaller thickness, which make the structure more compliant. These features are combined in a single example so that the coupling between fluid and structure exhibits stronger strength in comparison with previous cases. The present example therefore seeks to assess the application of the novel GBMS and WFEM to an even more complex case, aiming to appraise potential limitations.

The external dimensions of the unit cell are taken as $60\,\mathrm{mm} \times 10\,\mathrm{mm} \times 30\,\mathrm{mm}$ (same as those considered in Section 5.1 and Appendix A.1). Additionally, the thickness of all walls is reduced to 1 mm, which leads to the fluid cavity measuring $58\,\mathrm{mm} \times 8\,\mathrm{mm} \times 28\,\mathrm{mm}$. The latter is connected to adjacent unit cells through rectangular communicating channels of $4\,\mathrm{mm} \times 16\,\mathrm{mm}$, with 1 mm depth, at the unit cell's left and right interfaces, similar to the case addressed in Section A.1. The previous description already characterizes the complete geometry of the unit cell, which resembles the one shown in Fig. 18. It has been modified, nevertheless, following the procedures adopted in Section 5.2 and Appendix A.2, to render it asymmetric, as well. In particular, the baseline geometry was shifted along the direction of wave propagation by $\Delta/3$, i.e., $33.\overline{3}$ % of the unit cell length, as can be seen in Fig. 23.

One recalls that in all other examples the maximum frequency considered to perform analyses was taken as 5000 Hz. For the current unit cell, however, this showed to be impractical. For instance, it is much more flexible in comparison to previous geometries, such that hundreds of free-free vibration modes result between 0 and 5000 Hz for an assembly made with $N = 6$ unit cells. In essence, analyzing the unit cell now considered in this whole frequency range becomes problematic using the proposed MOR strategy since it is unable to reduce the model to an amenable size. While this fact does not appear troublesome, in reality a large number of DoFs become necessary at the left and right boundaries of the unit cell reduced-model, which compromises accurate computation of highly evanescent wave modes—a fact that is further complicated due to Δ being "large", its reduction not being possible. Furthermore, convergence of the unit cell (free-free) natural frequencies up to 5000 Hz is in itself challenging due to its ultra-flexible behavior, a consequence of its thinner walls, requiring a very fine mesh, with more than a hundred thousand DoFs. Whilst this could be pursued, to remediate the inaccurate computation of highly evanescent wave-modes, one possibility would involve recurring to higher or mixed precision floating-point arithmetic calculations, something that has not been undertaken in this study. Instead, one has simply reduced $f_{\max}$ to 1000 Hz and Δ_f to 1 Hz for this example. One notes that the FE mesh of a single unit cell of the acousto-elastic periodic structure addressed here, shown in Fig. 23, has been constructed to ensure convergence of the largest natural frequency of the unit cell that lies between 0 and $f_{\max}$ (equal to 1000 Hz for this example). Looking at Table 11, which presents data concerning the mesh convergence analysis that has been performed, one sees that the ES = 1.5 mm which has been used for simulations should ensure correct results.

Data related to the reduced-order model obtained for the unit cell shown in Fig. 23, employing $n_{\mathrm{CB}} = 5$, $n_{\mathrm{L\text{-}CC_I}} = 5$, $n_{\mathrm{L\text{-}CC_B}} = 2$, and $\tau = 0.8$, in accordance with Section 4.1, is presented in Table 12. As one may notice from its inspection, single fixed-interface modes are employed for the $\mathrm{U_I}$ and $\mathrm{P_I}$ DoF sets in the modal model. The number of DoFs located internally at the FSI, namely in the set Γ_{I}, drops from 33072 to 430, whereas the

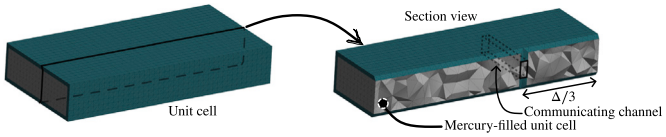

Fig. 23. Finite element mesh and section view of a unit cell of the periodic structure incorporating a heavier fluid (mercury), a communicating channel, thinner walls, and an asymmetric design (dimensions are indicated in the text).

Table 11
Convergence analysis of the largest natural frequency of the unit cell shown in Fig. 23 that lies between 0 and f_{max} (equal to 1000 Hz) and is associated with the same eigenvector.

ES (mm)	Natural frequency (Hz)	RE (%)
2.5	1019.3	–
2.0	1000.9	1.84
1.5	985.0	1.61

Table 12
Number of physical and modal DoFs for the unit cell FE model shown in Fig. 23.

	Set of DoFs									
	U_L	P_L	Γ_L	U_R	P_R	Γ_R	U_I	P_I	Γ_I	Total
Full-order model	636	407	400	636	407	400	52389	10751	33072	99098
Reduced-order model ($n_{CB} = 5$, $n_{L\text{-}CC_I} = 5$, $n_{L\text{-}CC_B} = 2$, and $\tau = 0.8$)	45	22	85	45	22	85	1	1	430	736

boundary DoFs decrease from 2×1443 to 2×152. Overall, 99098 physical DoFs were replaced by 736 generalized coordinates, corresponding to a reduction of the model size by a factor of more than 130.

Considering the finite acousto-elastic periodic structure is assembled with $N = 6$ unit cells, and that the harmonic input force and responses are related to locations analogous to those indicated in Fig. 3, FRFs have been obtained using the proposed modeling framework. The results are presented in Fig. 24, together with reference FRFs obtained by the FEM, as well as their respective REs and CSFs. One can see that the accelerance and acoustic FRFs computed using the WFEM closely match those calculated by the FEM. In fact, the REs between the resonance frequencies predicted by the FEM and the WFEM remain lower than 1% for all resonances, whereas the CSFs between the FRFs stay predominantly equal to one throughout the entire frequency band, demonstrating the reduced-order model can accurately replace the full-order one.

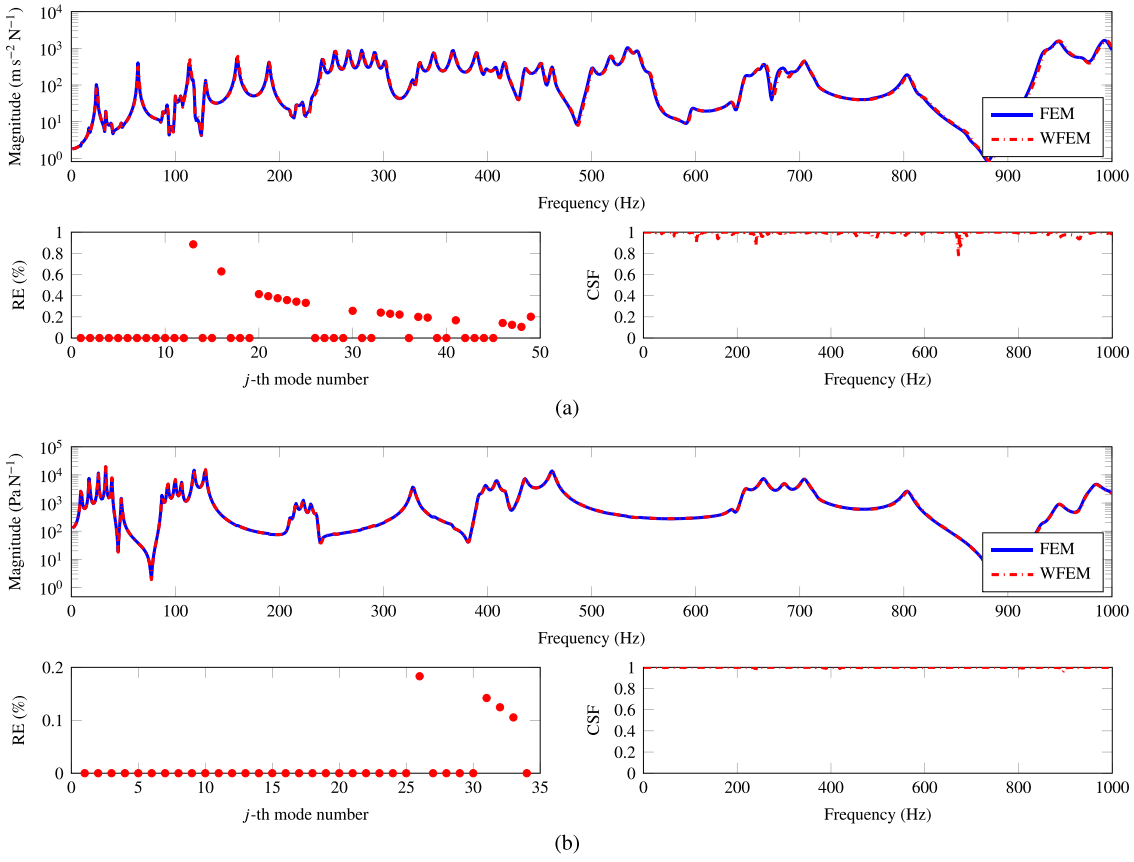

Fig. 24. Magnitude of a) accelerance and b) pressure FRFs for a finite acousto-elastic periodic structure, as shown in Fig. 3 but considering the unit cell model from Fig. 23, computed using the FEM and WFEM, along with the corresponding REs and CSFs. For the WFEM, a reduced-order model was employed, with $n_{CB} = 5$, $n_{L\text{-}CC_I} = 5$, $n_{L\text{-}CC_B} = 2$, and $\tau = 0.8$.

A.4. Summary

The previous sections of this appendix have considered three different periodic structures seeking to assess the applicability of the novel GBMS and WFEM to complementary systems beyond those discussed in Sections 4 and 5, potentially showing stronger fluid–structure interaction.

The reduced-order models obtained for systems considered in Appendices A.1–A.3 all have in common the fact that single structural and acoustic fixed-interface modes were used to describe uncoupled internal DoFs (U_I and P_I DoF sets). As explained in the main body of the paper, significant DoF reduction for these sets occurs owing to the fact that the unit cell FSIs and boundary DoFs are preserved during step **(2)** shown in Fig. 1. This makes the ensuing models stiffer, with higher natural frequencies, which ultimately leads to the aforementioned outcome. One recalls that this does not allow for the use of a coarse mesh in the interior domain of unit cells, as it can also comprise FSIs, whose dynamic behavior necessitates more modal DoFs for being properly modeled.

The results in the previous sections indicate that the proposed modeling framework can be applied to a range of problems with diverse complexity, such as: i) acousto-elastic periodic structures with heavy fluid; ii) both symmetric and asymmetric unit cell designs; and iii) lattices composed of unit cells that are more compliant, with thinner walls. In particular, the outcomes from Appendices A.2 and A.3 highlight that the MAC-based boundary-mode selection procedure is not limited to symmetric unit cell geometries. In fact, it can be applied to symmetric or asymmetric unit cells, with symmetric or asymmetric FE meshes, with the only requirement being to set a threshold value for τ that proves suitable for distinguishing the so-called redundant modes for their proper exclusion.

In addition, the results in Appendices A.1–A.3 demonstrate that the proposed modeling framework works very well for periodic structures with stronger fluid–structure interactions. In all cases, the REs and CSFs between the WFEM results and the FEM-reference ones remained lower than 2% (mostly lower than 0.6%) and very close to one, respectively, demonstrating that highly accurate reduced-order models with relatively few DoFs can replace their full-order counterparts, which contain several thousands of DoFs, by adopting the modeling framework introduced in this work. In fact, extremely size-reduced acousto-elastic modal models have been obtained with the novel GBMS, reaching reduction rates of up to 135, with less than 0.8% of the number of physical DoFs.

Although only phononic-like geometries were considered as additional examples in this appendix, the MOR framework introduced in this study also applies to locally resonant acousto-elastic periodic structures. Results related to such systems were not included in the manuscript due to length constraints.

Data availability

Data will be made available on request.

References

[1] Yuan Y, Wang H. Dual tunability in flexural and torsional bandgaps for pipe systems using perforated auxetic rings. Int J Solids Struct 2026;326:113747. https://doi.org/10.1016/j.ijsolstr.2025.113747

[2] Collet M, Ouisse M, Tateo F. Adaptive metacomposites for vibroacoustic control applications. In: IEEE sensors J, vol. 14; 2014. p. 2145–52. https://doi.org/10.1109/jsen.2014.2300052

[3] Tikani V, Ziaei-Rad S. Optimization and experimental validation of anti-tri chiral lattice metamaterial for broadband vibration suppression. Int J Solids Struct 2025;316:113384. https://doi.org/10.1016/j.ijsolstr.2025.113384

[4] Barbosa A, Kacem N, Bouhaddi N. A design methodology for nonlinear oscillator chains enabling energy localization tuning and soliton stability enhancement with optimal damping, mech. Syst. Signal Pr. 2024;213:111358. https://doi.org/10.1016/j.ymssp.2024.111358

[5] Hussein MI, Leamy MJ, Ruzzene M. Dynamics of phononic materials and structures: historical origins, recent progress, and future outlook. Appl Mech Rev 2014;66:040802. https://doi.org/10.1115/1.4026911

[6] Miranda Jr. EJP, Nobrega ED, Rodrigues SF, Aranas Jr. C, Santos JMCD. Wave attenuation in elastic metamaterial thick plates: analytical, numerical and experimental investigations. Int J Solids Struct 2020;204–5:138–52. https://doi.org/10.1016/j.ijsolstr.2020.08.002

[7] Li J-B, Wang Y-S, Zhang C. Dispersion relations of a periodic array of fluid-filled holes embedded in an elastic solid. J Comput Acoust 2012;20:1250014. https://doi.org/10.1142/s0218396x12500142

[8] Santos VMS, Martins YAD, Santos HEAA, Sales TP, Rade DA. Stochastic modeling of periodic beams under uncertain boundary conditions and environmental fluctuations. Int J Mech Sci 2025;285:109779. https://doi.org/10.1016/j.ijmecsci.2024.109779

[9] Patel H, Chen J, Hu Y, Erturk A. Photo-responsive hydrogel-based re-programmable metamaterials, sci. Rep. 2022;12:13033. https://doi.org/10.1038/s41598-022-15453-7

[10] Dudek KK, Mizzi L, Martínez JAI, Spaggiari A, Ulliac G, Gatt R, Grima JN, Laude V, Kadic M. Micro-scale graded mechanical metamaterials exhibiting versatile poisson's ratio, compos. Struct. 2023;319:117151. https://doi.org/10.1016/j.compstruct.2023.117151

[11] Shen Y, Lacarbonara W. Wave propagation and multi-stopband behavior of metamaterial lattices with nonlinear locally resonant membranes. Int. J. Non Linear Mech. 2024;161:104671. https://doi.org/10.1016/j.ijnonlinmec.2024.104671

[12] Waki Y, Mace BR, Brennan MJ. Numerical issues concerning the wave and finite element method for free and forced vibrations of waveguides. J Sound Vib 2009;327:92–108. https://doi.org/10.1016/j.jsv.2009.06.005

[13] Hoang T, Duhamel D, Foret G. Wave finite element method for waveguides and periodic structures subjected to arbitrary loads, finite elem. Anal. Des. 2020;179:103437. https://doi.org/10.1016/j.finel.2020.103437

[14] Duhamel D, Mencik J-M. Reduced-order modeling for time domain analysis of finite periodic structures with absorbing boundary conditions. J Sound Vib 2024;590:118576. https://doi.org/10.1016/j.jsv.2024.118576

[15] Mencik J-M. On the low- and mid-frequency forced response of elastic structures using wave finite elements with one-dimensional propagation, comput. Struct. 2010;88:674–89. https://doi.org/10.1016/j.compstruc.2010.02.006

[16] Mencik J-M, Duhamel D. A wave-based model reduction technique for the description of the dynamic behavior of periodic structures involving arbitrary-shaped substructures and large-sized finite element models, finite elem. Anal. Des. 2015;101:1–14. https://doi.org/10.1016/j.finel.2015.03.003

[17] Santos VMS, Sales TP, Ouisse M. Improving the computation of forced responses of periodic structures by the wave-based finite element method via a modified generalized Bloch mode synthesis, finite elem. Anal. Des. 2025;245:104314. https://doi.org/10.1016/j.finel.2025.104314

[18] Hurty WC. Vibrations of structural systems by component mode synthesis. J Eng Mech Div 1960;86:51–69. https://doi.org/10.1061/jmcea3.0000162

[19] Craig Jr. RR, Bampton MCC. Coupling of substructures for dynamic analyses. AIAA J 1968;6:1313–9. https://doi.org/10.2514/3.4741

[20] Krattiger D, Hussein MI. Bloch mode synthesis: ultrafast methodology for elastic band-structure calculations. Phys Rev E 2014;90:063306. https://doi.org/10.1103/physreve.90.063306

[21] Krattiger D, Hussein MI. Generalized Bloch mode synthesis for accelerated calculation of elastic band structures. J Comput Phys 2018;357:183–205. https://doi.org/10.1016/j.jcp.2017.12.016

[22] Palermo A, Marzani A. Extended Bloch mode synthesis: ultrafast method for the computation of complex band structures in phononic media. Int J Solids Struct 2016;100–101:29–40. https://doi.org/10.1016/j.ijsolstr.2016.06.033

[23] Aladwani A. A refined Bloch mode synthesis framework for fast and accurate analysis of electroelastic metamaterials with piezoelectric resonant shunt damping, mech. Syst. Signal Pr. 2022;180:109380. https://doi.org/10.1016/j.ymssp.2022.109380

[24] Aladwani A, Nouh M, Hussein MI. State-space Bloch mode synthesis for fast band-structure calculations of non-classically damped phononic materials, comput. Method. Appl. M. 2022;396:115018. https://doi.org/10.1016/j.cma.2022.115018

[25] Jiang D, Zhang S, Li Y, Chen B, Li N. A hybrid Bloch mode synthesis method based on the free interface component mode synthesis method. J Comput Phys 2024;496:112556. https://doi.org/10.1016/j.jcp.2023.112556

[26] Cool V, Naets F, Van Belle L, Desmet W, Deckers E. Accelerated dispersion curve calculations for periodic vibro-acoustic structures, front. Mech. Eng. 2022;8:995322. https://doi.org/10.3389/fmech.2022.995322

[27] Xi C, Zheng H. Improving the generalized Bloch mode synthesis method using algebraic condensation, comput. Method. Appl. M. 2021;379:113758. https://doi.org/10.1016/j.cma.2021.113758

[28] Zhu X, Xi C, Zheng H. An improvement of generalized Bloch mode synthesis method-based model order reduction technique for band-structure computation of periodic structures, comput. Struct. 2023;281:107013. https://doi.org/10.1016/j.compstruc.2023.107013

[29] Boily S, Charron F. The vibroacoustic response of a cylindrical shell structure with viscoelastic and poroelastic materials, appl. Acoust. 1999;58:131–52. https://doi.org/10.1016/s0003-682x(98)00070-x

[30] Tran QH, Ouisse M, Bouhaddi N. A robust component mode synthesis method for stochastic damped vibroacoustics, mech. Syst. Signal Pr. 2010;24:164–81. https://doi.org/10.1016/j.ymssp.2009.06.016

[31] Kim SM, Kim J-G, Chae S-W, Park KC. A strongly coupled model reduction of vibro-acoustic interaction, comput. Method. Appl. M. 2019;347:495–516. https://doi.org/10.1016/j.cma.2018.12.029

[32] Claro DS, Denis V, Mencik J-M. A wave finite element approach for the vibroacoustic analysis of fluid-filled pipes with joints and defects. Wave Motion 2025;138:103576. https://doi.org/10.1016/j.wavemoti.2025.103576
[33] Wei Q, Xiang J, Zhu W, Hu H. Band structure calculations of three-dimensional solid-fluid coupling phononic crystals using dual reciprocity boundary element method and wavelet compression method. Comput Phys Commun 2024;299:109165. https://doi.org/10.1016/j.cpc.2024.109165
[34] Aladwani A, Almandeel A, Nouh M. Fluid-structural coupling in metamaterial plates for vibration and noise mitigation in acoustic cavities. Int J Mech Sci 2019;152:151–66. https://doi.org/10.1016/j.ijmecsci.2018.12.048
[35] Maess M, Gaul L. Substructuring and model reduction of pipe components interacting with acoustic fluids, mech. Syst. Signal Pr. 2006;20:45–64. https://doi.org/10.1016/j.ymssp.2005.02.008
[36] Herrmann J, Maess M, Gaul L. Substructuring including interface reduction for the efficient vibro-acoustic simulation of fluid-filled piping systems, mech. Syst. Signal Pr. 2010;24:153–63. https://doi.org/10.1016/j.ymssp.2009.05.003
[37] Santos VMS, Sales TP, Ouisse M. Dynamic behavior of acousto-elastic phononic crystals incorporating fluid sloshing and communicating channels between unit cells. In: Proc. XX Int. Symp. Dynamic Probl. Mech; 2025. p. 1–10. https://hal.science/hal-05322159v1.
[38] Cool V, Boukadia R, Van Belle L, Desmet W, Deckers E. Contribution of the wave modes to the sound transmission loss of inhomogeneous periodic structures using a wave and finite element based approach. J Sound Vib 2022;537:117183. https://doi.org/10.1016/j.jsv.2022.117183
[39] Cool V, Sigmund O, Aage N. Metamaterial design with vibroacoustic bandgaps through topology optimization, comput. Method. Appl. M. 2025;436:117744. https://doi.org/10.1016/j.cma.2025.117744
[40] Elmadih W, Chronopoulos D, Zhu J. Metamaterials for simultaneous acoustic and elastic bandgaps. Sci Rep 2021;11:14635. https://doi.org/10.1038/s41598-021-94053-3
[41] Gugercin S. An iterative SVD-krylov based method for model reduction of large-scale dynamical systems. Linear Algebra Appl. 2008;428:1964–86. https://doi.org/10.1016/j.laa.2007.10.041
[42] Hernández JA, Caicedo MA, Ferrer A. Dimensional hyper-reduction of nonlinear finite element models via empirical cubature, comput. Method. Appl. M. 2017;313:687–722. https://doi.org/10.1016/j.cma.2016.10.022
[43] Maierhofer J, Rixen DJ. Model order reduction using hyperreduction methods (DEIM, ECSW) for magnetodynamic FEM problems, finite elem. Anal. Des. 2022;209:103793. https://doi.org/10.1016/j.finel.2022.103793
[44] Hoareau C, Deü J-F, Ohayon R. Construction of reduced order operators for hydroelastic vibrations of prestressed liquid-structure systems using separated parameters decomposition, comput. Method. Appl. M. 2022;402:115406. https://doi.org/10.1016/j.cma.2022.115406
[45] MATLAB, version 24.2.0.2712019 (R2024b). The MathWorks Inc. orth; 2024. URL: https://www.mathworks.com/help/matlab/ref/orth.html [Accessed 23 January 2025].
[46] Smida BB, Majed R, Bouhaddi N, Ouisse M. Investigations for a model reduction technique of fluid-structure coupled systems, proc. Inst. Mech. Eng. C 2011;226:42–54. https://doi.org/10.1177/0954406211411863
[47] Cool V, Naets F, Van Belle L, Desmet W, Deckers E. Efficient dispersion curve computations for periodic vibro-acoustic structures using the (generalized) Bloch mode synthesis. In: Proc. of ECCOMAS; 2022. p. 1–8. https://doi.org/10.23967/eccomas.2022.104
[48] Ma Z-D, Hagiwara I. Sensitivity analysis methods for coupled acoustic-structural systems Part I: Modal sensitivities. AIAA J 1991;29:1787–95. https://doi.org/10.2514/3.61525
[49] Wyckaert K, Augusztinovicz F, Sas P. Vibro-acoustical modal analysis: reciprocity, model symmetry, and model validity. J Acoust Soc Am 1996;100:3172–81. https://doi.org/10.1121/1.417127
[50] Oliveira LPR, Silva MM, Sánchez JAM, Gonçalves LAM. Loudness scattering due to vibro-acoustic model variability. J. Braz. Soc. Mech. Sci. & Eng. 2012;34:604–11. https://doi.org/10.1590/s1678-58782012000600009
[51] Creixell-Mediante E, Jensen JS, Brunskog J, Larsen M. Model reduction for optimization of structural-acoustic coupling problems. In: Proc. of ISMA; 2016. p. 3913–28.
[52] Krattiger D, Wu L, Zacharczuk M, Buck M, Kuether RJ, Allen MS, Tiso P, Brake MRW. Interface reduction for Hurty/Craig-Bampton substructured models: review and improvements, mech. Syst. Signal Pr. 2019;114:579–603. https://doi.org/10.1016/j.ymssp.2018.05.031
[53] Mencik J-M, Ichchou MN. Multi-mode propagation and diffusion in structures through finite elements. Eur. J. Mech. A. Solids 2005;24:877–98. https://doi.org/10.1016/j.euromechsol.2005.05.004
[54] Everstine GC. A symmetric potential formulation for fluid-structure interaction. J Sound Vib 1981;79:157–60. https://doi.org/10.1016/0022-460x(81)90335-7
[55] Santos VMS, Sales TP, Ouisse M. Investigation of a novel metastructure with trapped, fluid-filled unit cells. In: Kurka P, Pereira M, editors. Advances in structural Vibration. Lecture notes in mechanical engineering. Springer; 2025. p. 111–26. https://doi.org/10.1007/978-3-031-71540-2_9
[56] Santos VMS, Sales TP. Numerical investigation of a zig-zag beam-type quasi-periodic structure with multiple defects. In: Proc. XIX Int. Symp. Dynamic Probl. Mech. DIN2023. ABCM; 2023. p. 1–10. https://doi.org/10.26678/abcm.dname2023.din2023-0170
[57] Santos VMS. Numerical investigation of wave propagation in beams coupled to metastructures combining spectral and wave-finite element methods [Master's thesis]. Aeronautics Institute of Technology; 2022.
[58] Van hoorickx C, Reynders EPB. Coupling strength evaluation in vibro-acoustic systems. J Sound Vib 2022;536:117133. https://doi.org/10.1016/j.jsv.2022.117133
[59] Mencik J-M, Ichchou MN. Wave finite elements in guided elastodynamics with internal fluid. Int J Solids Struct 2007;44:2148–67. https://doi.org/10.1016/j.ijsolstr.2006.06.048
[60] Maess MK, Gaul L. Simulation of structural deformations of flexible piping systems by acoustic excitation. J. Pressure Vessel Technol. 2007;129:363–71. https://doi.org/10.1115/1.2748819
[61] Mencik J-M. New advances in the forced response computation of periodic structures using the wave finite element (WFE) method, comput. Mech. 2014;54:789–801. https://doi.org/10.1007/s00466-014-1033-1
[62] Miller HR. Optimization: foundations and applications. Wiley; 2011.
[63] Silva TAN, Maia NMM, Barbosa JI. A model updating technique based on FRFs for damped structures. In: Proc. of ISMA; 2012. p. 2213–26.
[64] Guillaume P, Verboven P, Vanlanduit S, Van der Auweraer H, Peeters B. A poly-reference implementation of the least-squares complex frequency-domain estimator. In: Proc. of IMAC; 2003. p. 1–9.
[65] Kontou E, Charitos I, Drougkas A. Modeling the fundamental viscoelastic properties of polylactic acid (PLA) and PLA/Nanocomposites in a unified manner. Nanomaterials 2024;14:1116. https://doi.org/10.3390/nano14131116
[66] Zohdi N, Yang RC. Material anisotropy in additively manufactured polymers and polymer composites: a review. Polymers 2021;13:3368. https://doi.org/10.3390/polym13193368